

# An efficient numerical method for RANS/LES turbulent simulations using subfilter scale stress transport equations

Bruno Chaouat\*

*ONERA , 92322 Châtillon, France*

## Abstract

We propose a numerical method for performing hybrid non-zonal RANS/LES simulations by using a subfilter scale stress transport model in the framework of finite volume technique. The turbulent equations are derived from the new partial integrated transport modeling (PITM) method. The PITM method has been initially developed for devising subfilter energy models based on the viscosity concept [1] and has been then extended to subfilter stress models relying on second moment closures [2, 3, 4]. The numerical method put in place is developed in a general framework of large eddy simulations and can be applied to almost all subfilter-scale models based on transport equations of subfilter scale turbulent quantities. In this work, we have developed specific numerical schemes for solving the turbulent transport equations of compressible flows including the density, velocity, energy, subfilter scale turbulent stresses and subfilter scale dissipation-rate that are strongly coupled together. When performing LES or VLES simulations, this coupling between the motion and turbulent equations poses some numerical problems because the subfilter scale turbulent stresses and dissipation-rate are more fluctuating in time and space than in the case of RANS computations, so that a specific numerical treatment has been proposed. In this framework, new implicit iterative algorithms in time are especially developed for solving the unsteady equations of the turbulent energy, stresses and dissipation-rate by ensuring the positivity of the normal stresses at each step of the computation. We show that the convective fluxes resulting from the volume technique including the main and turbulent variables can be computed by an approximate Riemann solver using new tensorial operators. The numerical solver is calibrated on the decay of isotropic spectrum and on the well known fully turbulent channel flow for assessing the performances of the numerical method. Then, we perform numerical simulations of the turbulent channel flow over periodic hills on coarse and medium grids. This flow encountered in aeronautical applications is of complex physics because governed by interacting turbulence mechanisms associated with separation, recirculation and reattachment. As a result, it is found that the proposed numerical method used in conjunction with the subfilter stress model performs fairly well these turbulent flows on different grids. From a practical point of view, this numerical method can be easily implemented in CFD codes for tackling engineering applications.

---

\*Senior Scientist, Department of Computational Fluid Dynamics. E-mail address: Bruno.Chaouat@onera.fr

# 1 Introduction

Turbulence modeling methods including both RANS (Reynolds averaged Navier-Stokes) equations and LES (large eddy simulations) have made significant progress in the past two-decades for predicting turbulent flows [5]. RANS method consists of modeling the whole energy spectrum including all the turbulent scales whereas LES simulation only requires to model the region of the spectrum located after the cutoff wave number. Usually, numerical RANS or LES flow simulations are performed by using eddy-viscosity turbulence models because of their simple formulations [6, 7, 8]. Although these models perform well for shear flows where the shear stress is the most important dynamical component of the stress tensor, a reliable prediction of normal turbulent stresses is required, particularly for aeronautical or turbomachinery applications [9, 10]. In this framework, second-order closure models have been developed to overcome the deficiencies of first-order closure models. Indeed, second-order closure models account for more physics than viscosity models. They allow to reproduce turbulent flows involving complex physics phenomena produced by strong effects of streamline curvature such as detachment or reattachment of the boundary layer, separation and recirculation in presence of adverse pressure gradient, as well as rotational effects. Transport turbulent stress models based on second-moment closure level have been used in both RANS [11, 12, 13, 14] and LES [15, 2, 3] methodologies. If these models are sophisticated, they are however not widely used in industry despite their advantages. The main reason arises from the mathematical complexity of solving these equations which are strongly coupled together leading to a lack of robustness of the numerical scheme [16]. More precisely, the origin of the problem lies in the coupling between the mean velocity and the turbulent stress field as well as the coupling between the stresses and dissipation-rate equations. In two-equation eddy-viscosity models, the turbulence stresses are usually treated as diffusion terms that have the effect to stabilize the momentum equations whereas in second-moment closures, the stresses are mainly integrated as source terms that have a destabilizing effect on the motion equations. Indeed, for high Reynolds number flows where the viscous terms are negligible, the momentum equations are then dominated by the source terms which are supplied from separate transport equations. This problem is made worse when performing hybrid RANS/LES simulations because the stresses are more fluctuating in time and space. Moreover, in two-equation eddy-viscosity models, the production term of the turbulent energy is always positive as a consequence of the Boussinesq hypothesis whereas for second-moment closures, the tensorial production term associated with each individual stress component may appear as source or sink. Because of these problems encountered in second-moment closures, the positivity of the normal stresses is not guaranteed if the numerical scheme is not appropriate, even if the turbulence model is realizable from a physical standpoint. Finally, the last point usually invoked that dissuades researchers to apply second-moment closures is the expected considerable increase of the computational cost required for solving seven equations (stresses  $\tau_{ij}$  and dissipation-rate  $\epsilon$ ) instead of two equations (energy  $k$  and  $\epsilon$ ) [17]. This argument is indeed often used by practitioners although not always justified from a numerical point of view. In fact, the increase of the CPU cost is mainly related to the code programming where the vectorization and/or the parallelization techniques are of major importance.

Both RANS and LES approaches have their own numerical methods. For highly resolved LES

simulations, spectral methods [18, 19] or high order finite difference methods in space discretization [20] are usually used whereas for RANS computations, the finite volume technique [21] with numerical upwind schemes of second-order accuracy in space discretization is rather considered. In the framework of finite volume technique, numerical RANS solvers with second-moment turbulence closures have been developed so that one can reasonably think that they can also be used in LES methodology. But this is not the case because the solver must be able to accurately compute the large scales without any numerical dissipation and must be particularly robust for solving unsteady equations that are very fluctuating in time and space. This point is essential when performing LES simulations. In these conditions, only specific schemes with stabilization techniques can be applied for solving the system of both the mean and turbulent transport equations. This constitutes the main objective of this present work.

We propose a new numerical method for performing hybrid non-zonal RANS/LES simulations by using a subfilter stress model in the framework of finite volume technique, the turbulent equations being derived from the partial integrated transport modeling (PITM) method [1, 2, 3]. This is a general numerical method which can be applied to almost all subfilter-scale models based on transport equations of subfilter scale turbulent quantities. In this work, the equations are integrated in time by a Runge-Kutta scheme of fourth order accuracy. New implicit iterative algorithms are especially developed for solving the subfilter scale turbulent stress and subfilter-scale dissipation-rate equations by ensuring the positivity of the normal stresses at each step of the computation. We propose also a numerical scheme in space discretization for accurately computing the large scales of flows. The convective fluxes resulting from the volume technique are computed by an approximate Riemann solver using tensorial operators. It is found as a result that the Jacobian matrix can be developed under an original spectral tensorial form. With regard to conventional methods, we show that this approach reduces the computational cost. Some test cases are then presented for calibrating the numerical solver and for illustrating the potentialities of the numerical method put in place.

## 2 Governing equations

### 2.1 Mean flow equations

In this section, we present briefly the system of the main and turbulent transport equations for a turbulent compressible flow of a viscous fluid. For hybrid RANS/LES simulations, the instantaneous flow variable  $\phi$  is decomposed into a filtered part and a subfilter-scale fluctuating part. The Favre averaging is used for compressible flows leading to the following decomposition  $\phi = \tilde{\phi} + \phi''$  where the quantities  $\tilde{\phi} = \overline{\rho\phi}/\bar{\rho}$  and  $\phi'' = \phi' + \bar{\phi} - \tilde{\phi}$  denote the mean and the fluctuating contributions of the variable  $\phi$ , respectively. The filtering of the instantaneous Navier-Stokes equations produces in Favre variables the equations for the mean density  $\bar{\rho}$ , the mean momentum  $\bar{\rho}\tilde{u}_i$ , and the mean energy  $\bar{\rho}\tilde{E}$  as follows

$$\frac{\partial \bar{\rho}}{\partial t} + \frac{\partial}{\partial x_j} (\bar{\rho}\tilde{u}_j) = 0 \quad (1)$$

$$\frac{\partial}{\partial t}(\bar{\rho} \tilde{u}_i) + \frac{\partial}{\partial x_j}(\bar{\rho} \tilde{u}_i \tilde{u}_j + \bar{p} \delta_{ij}) = \frac{\partial \bar{\sigma}_{ij}}{\partial x_j} - \frac{\partial}{\partial x_j}(\bar{\rho} (\tau_{ij})_{sfs}) \quad (2)$$

and

$$\frac{\partial}{\partial t}(\bar{\rho} \tilde{E}) + \frac{\partial}{\partial x_j}(\bar{\rho} \tilde{H} \tilde{u}_j) = \frac{\partial}{\partial x_j}(\tilde{\sigma}_{ij} \tilde{u}_i) - \frac{\partial q_j}{\partial x_j} \quad (3)$$

where  $\rho$ ,  $u_i$ ,  $p$ ,  $T$ ,  $E$ ,  $H$ ,  $\sigma_{ij}$ ,  $(\tau_{ij})_{sfs}$ ,  $q_i$ , are the density, velocity vector, pressure, temperature, total energy, total enthalpy, viscous stress tensor, subfilter scale turbulent stress tensor, total heat flux, respectively. In these equations, the viscous tensor  $\sigma_{ij}$  takes the usual form

$$\bar{\sigma}_{ij} \approx \bar{\mu} \left( \frac{\partial \tilde{u}_i}{\partial x_j} + \frac{\partial \tilde{u}_j}{\partial x_i} \right) - \frac{2}{3} \bar{\mu} \frac{\partial \tilde{u}_m}{\partial x_m} \delta_{ij} \quad (4)$$

where  $\mu$  stands for the molecular viscosity. The subfilter turbulent stress tensor  $(\tau_{ij})_{sfs}$ , the total energy  $\tilde{E}$ , and the total enthalpy  $\tilde{H}$  are defined by the mathematical relations

$$(\tau_{ij})_{sfs} = \widetilde{u_i u_j} - \tilde{u}_i \tilde{u}_j, \quad (5)$$

$$\tilde{E} = c_v \tilde{T} + \frac{\tilde{u}_m \tilde{u}_m}{2} + \frac{(\tau_{mm})_{sfs}}{2}, \quad (6)$$

$$\tilde{H} = \tilde{E} + \frac{\bar{p}}{\bar{\rho}}, \quad (7)$$

where  $c_v$  is the specific heat capacity at constant volume. The total heat flux  $q_i$  includes the laminar and subfilter turbulent contributions

$$q_i = -(\lambda_T + c_\nu \bar{\rho} \frac{k_{sfs}^2}{\epsilon_{sfs}} \frac{c_p}{P_{rt}}) \frac{\partial \tilde{T}}{\partial x_i} \quad (8)$$

where  $\lambda_T$  is the thermal conductivity,  $c_p$  and  $P_{rt}$  are the specific heat at constant pressure and the turbulent Prandtl number, respectively,  $k_{sfs} = (\tau_{mm})_{sfs}/2$  and  $\epsilon_{sfs}$  denotes the subfilter dissipation-rate,  $c_\nu = 0.09$ . Assuming ideal gas law  $p = \rho R T / \mathcal{M}$ , where  $R$  is the gas constant and  $\mathcal{M}$  the molar mass, and constant heat capacity  $c_p$ , the mean thermodynamic pressure is computed by the equation

$$\bar{p} = (\gamma - 1) \bar{\rho} \left( \tilde{E} - \frac{\tilde{u}_m \tilde{u}_m}{2} - \frac{(\tau_{mm})_{sfs}}{2} \right) \quad (9)$$

where  $\gamma = c_p/c_v$  is the ratio of specific heats. Closure of the momentum equation is necessary for the subfilter turbulent stress tensor  $(\tau_{ij})_{sfs} = \widetilde{u_i u_j} - \tilde{u}_i \tilde{u}_j$  which is modeled by means of its transport equation.

## 2.2 Subfilter scale stress and dissipation-rate equations

We present briefly the basic form of the subfilter scale stress and dissipation-rate equations. The modeling of these equations for LES simulations has been conducted in references [2, 3, 4] by the PITM method and is beyond the scope of the present paper focused on numerical methods. As

a result, the transport equation of the subfilter turbulent stress is written in the simple compact form as

$$\frac{D(\bar{\rho}(\tau_{ij})_{sfs})}{Dt} = P_{ij} + \Psi_{ij} + J_{ij} - \bar{\rho}(\epsilon_{ij})_{sfs} \quad (10)$$

where  $D$  denotes the operator  $D(\bar{\rho}\phi)/Dt = \partial(\bar{\rho}\phi)/\partial t + \partial(\bar{\rho}\tilde{u}_j\phi)/\partial x_j$ . The terms appearing in the right-hand side of this equation are identified as production, redistribution, diffusion and dissipation, respectively. The transport equation for the subfilter turbulent energy is obtained as half the trace of equation (10)

$$\frac{D(\bar{\rho}k_{sfs})}{Dt} = P_k + J_k - \bar{\rho}\epsilon_{sfs} \quad (11)$$

where  $P_k = P_{mm}/2$ ,  $J_k = J_{mm}/2$ ,  $\epsilon_{sfs} = (\epsilon_{mm})_{sfs}/2$ . The production term  $P_{ij}$  is composed by the interaction between the stresses and the gradient velocities

$$P_{ij} = -\bar{\rho}(\tau_{ik})_{sfs} \frac{\partial \tilde{u}_j}{\partial x_k} - \bar{\rho}(\tau_{jk})_{sfs} \frac{\partial \tilde{u}_i}{\partial x_k} \quad (12)$$

The redistribution term  $\Psi_{ij}$  is decomposed into a slow part  $\Psi_{ij}^1$ , a rapid part,  $\Psi_{ij}^2$  and a wall reflection part  $\Psi_{ij}^3$ . The slow term  $\Psi_{ij}^1$  of Rotta characterizes the return to isotropy due to the action of turbulence on itself

$$\Psi_{ij}^1 = -c_1 \bar{\rho} \frac{\epsilon_{sfs}}{k_{sfs}} \left( (\tau_{ij})_{sfs} - \frac{1}{3} (\tau_{mm})_{sfs} \delta_{ij} \right), \quad (13)$$

the rapid term  $\Psi_{ij}^2$  of the isotropization of production involves the velocity gradients

$$\Psi_{ij}^2 = -c_2 \left( P_{ij} - \frac{1}{3} P_{mm} \delta_{ij} \right), \quad (14)$$

and the wall term  $\Psi_{ij}^3$  accounts for the wall effects [22]. The diffusion term  $J_{ij}$  is modeled assuming a gradient law hypothesis

$$J_{ij} = \frac{\partial}{\partial x_m} \left( \mu \frac{\partial (\tau_{ij})_{sfs}}{\partial x_m} + c_s \frac{\bar{\rho} k_{sfs}}{\epsilon_{sfs}} (\tau_{ml})_{sfs} \frac{\partial (\tau_{ij})_{sfs}}{\partial x_l} \right) = \frac{\partial j_{ijm}}{\partial x_m} \quad (15)$$

where  $c_s$  is a numerical coefficient set to 0.22. Closure of equation (10) needs the modeling of the tensorial subfilter dissipation-rate  $(\epsilon_{ij})_{sfs}$  or, assuming a local isotropy at high Reynolds number  $(\epsilon_{ij})_{sfs} = 2/3 \epsilon_{sfs} \delta_{ij}$ , the modeling of the scalar subfilter dissipation-rate  $\epsilon_{sfs}$ . The modeled transport equation  $\epsilon_{sfs}$  reads [1, 2, 3],

$$\frac{D(\bar{\rho}\epsilon_{sfs})}{Dt} = c_{\epsilon_1} \frac{\epsilon_{sfs}}{k_{sfs}} P_k - c_{sfs\epsilon_2} \bar{\rho} \frac{\epsilon_{sfs}^2}{k_{sfs}} + J_\epsilon \quad (16)$$

where  $c_{\epsilon_1} = 1.45$  and  $c_{sfs\epsilon_2}$  is a dynamical function of the dimensionless parameter  $\eta_c$  involving the ratio of the turbulent length-scale to the grid-size. This means that the subfilter stress model varies continuously from quasi URANS to LES model with respect to the function  $c_{sfs\epsilon_2}$  (see appendix A) [3]. In that sense, the PITM method is basically different from the unsteady RANS approach

although being compatible with it at the limit of vanishing cutoff. The diffusion term  $J_\epsilon$  appearing on the right hand side of equation (16) takes the expression

$$J_\epsilon = \frac{\partial}{\partial x_m} \left( \mu \frac{\partial \epsilon_{sfs}}{\partial x_m} + c_\epsilon \bar{\rho} \frac{k_{sfs}}{\epsilon_{sfs}} (\tau_{ml})_{sfs} \frac{\partial \epsilon_{sfs}}{\partial x_l} \right) = \frac{\partial j_{em}}{\partial x_m} \quad (17)$$

where the coefficient  $c_\epsilon$  is set to 0.18. The functional coefficients of the subfilter stress model are given in appendix A. The total Reynolds stress  $\tau_{ij}$  is calculated as the sum of the statistical average  $\langle . \rangle$  of the subfilter and large-scale parts. Assuming a spectral cutoff filter defined by the Fourier transform implying that the large and small scale fluctuations are uncorrelated [23, 24], the total stress reads [4]

$$\tau_{ij} = \langle (\tau_{ij})_{sfs} \rangle + \langle \tilde{u}_i \tilde{u}_j \rangle - \langle \tilde{u}_i \rangle \langle \tilde{u}_j \rangle \quad (18)$$

## 3 Numerical method

### 3.1 Finite volume technique

This section describes the numerical method. The present code [25] is based on the finite volume technique which is well suited for simulating aerodynamic flows in complex geometries. Considering the grid cell around the point  $(i, j, k)$ , the variation of the averaged unknown  $\mathbf{U}$  on the control volume  $v(\Omega)$  is then obtained by the following semi-discrete conservation equation

$$\frac{\partial \mathbf{U}}{\partial t} = -\frac{1}{v(\Omega)} \sum_{\sigma} (\mathbf{F} - \mathbf{F}_v) A_{\sigma} + \mathbf{S} \quad (19)$$

where  $\mathbf{F}$  and  $\mathbf{F}_v$  represent respectively the convective and viscous fluxes through the surfaces  $A_{\sigma}$  around the control volume  $v(\Omega)$ ,  $\mathbf{n}$  is the unit vector normal to the surface  $A_{\sigma}$  and  $\mathbf{S}$  is the source term. The mean variable  $\mathbf{U}$  is evaluated at the center of the volume whereas the fluxes are computed from the unknowns at the interfaces surrounding the volume. The expressions of the quantities  $\mathbf{U}$ ,  $\mathbf{F}$ ,  $\mathbf{F}_v$  and  $\mathbf{S}$ , written in compact form are the following

$$\mathbf{U} = \begin{bmatrix} \bar{\rho} \\ \bar{\rho} \tilde{u}_1 \\ \bar{\rho} \tilde{u}_2 \\ \bar{\rho} \tilde{u}_3 \\ \bar{\rho} \tilde{E} \\ \bar{\rho} (\tau_{11})_{sfs} \\ \bar{\rho} (\tau_{12})_{sfs} \\ \bar{\rho} (\tau_{13})_{sfs} \\ \bar{\rho} (\tau_{22})_{sfs} \\ \bar{\rho} (\tau_{23})_{sfs} \\ \bar{\rho} (\tau_{33})_{sfs} \\ \bar{\rho} \epsilon_{sfs} \end{bmatrix}, \quad \mathbf{F} = \begin{bmatrix} \bar{\rho} \tilde{u}_m n_m \\ \bar{\rho} \tilde{u}_1 \tilde{u}_m n_m + \bar{p} n_1 \\ \bar{\rho} \tilde{u}_2 \tilde{u}_m n_m + \bar{p} n_2 \\ \bar{\rho} \tilde{u}_3 \tilde{u}_m n_m + \bar{p} n_3 \\ \bar{\rho} \tilde{H} \tilde{u}_m n_m \\ \bar{\rho} (\tau_{11})_{sfs} \tilde{u}_m n_m \\ \bar{\rho} (\tau_{12})_{sfs} \tilde{u}_m n_m \\ \bar{\rho} (\tau_{13})_{sfs} \tilde{u}_m n_m \\ \bar{\rho} (\tau_{22})_{sfs} \tilde{u}_m n_m \\ \bar{\rho} (\tau_{23})_{sfs} \tilde{u}_m n_m \\ \bar{\rho} (\tau_{33})_{sfs} \tilde{u}_m n_m \\ \bar{\rho} \epsilon_{sfs} \tilde{u}_m n_m \end{bmatrix}, \quad \mathbf{F}_v = \begin{bmatrix} 0 \\ (\bar{\sigma}_{1m} - \bar{\rho} (\tau_{1m})_{sfs}) n_m \\ (\bar{\sigma}_{2m} - \bar{\rho} (\tau_{2m})_{sfs}) n_m \\ (\bar{\sigma}_{3m} - \bar{\rho} (\tau_{3m})_{sfs}) n_m \\ (\bar{\sigma}_{nm} \tilde{u}_n - q_m) n_m \\ j_{11m} n_m \\ j_{12m} n_m \\ j_{13m} n_m \\ j_{22m} n_m \\ j_{23m} n_m \\ j_{33m} n_m \\ j_{\epsilon m} n_m \end{bmatrix}$$

$$\mathbf{S} = \begin{bmatrix} 0 \\ 0 \\ 0 \\ 0 \\ 0 \\ P_{11} + \Psi_{11} - \frac{2}{3}\bar{\rho}\epsilon_{sfs} \\ P_{12} + \Psi_{12} \\ P_{13} + \Psi_{13} \\ P_{22} + \Psi_{22} - \frac{2}{3}\bar{\rho}\epsilon_{sfs} \\ P_{23} + \Psi_{23} \\ P_{33} + \Psi_{33} - \frac{2}{3}\bar{\rho}\epsilon_{sfs} \\ S_\epsilon \end{bmatrix}$$

Note that the transport equation (11) of the subfilter turbulent energy  $k_{sfs}$  is also integrated for numerical reasons although it is redundant from a physical point of view.

### 3.2 Time discretization

The vector  $\mathbf{U}$  is decomposed into the vector of mean variables  $\mathbf{U}_m = \bar{\rho} [1, \tilde{u}_1, \tilde{u}_2, \tilde{u}_3, \tilde{E}]^T$  and the vector of turbulent variables  $\mathbf{U}_t = \bar{\rho} [(\tau_{11})_{sfs}, (\tau_{12})_{sfs}, (\tau_{13})_{sfs}, (\tau_{22})_{sfs}, (\tau_{23})_{sfs}, (\tau_{33})_{sfs}, \epsilon_{sfs}]^T$ . A new combination of numerical schemes is proposed for solving in time the partial differential equations. Firstly, the convective and diffusive terms of the governing equations in conservative form are integrated explicitly in time using a fourth-order Runge-Kutta scheme

$$\mathbf{U}_m^{n+1} = \mathbf{U}_m^n + \delta t \sum_{k=1}^K \beta_k G(\mathbf{U}_m^{(k)}) \quad (20)$$

$$\mathbf{U}_t^{n+1} = \mathbf{U}_t^n + \delta t \sum_{k=1}^K \beta_k G(\mathbf{U}_t^{(k)}) \quad (21)$$

where  $\mathbf{U}_m^{(k)}$  and  $\mathbf{U}_t^{(k)}$  are defined by

$$\mathbf{U}_m^{(k)} = \mathbf{U}_m^n + \alpha_k \delta t G(\mathbf{U}_m^{(k-1)}) \quad (22)$$

and

$$\mathbf{U}_{t^*}^{(k)} = \mathbf{U}_t^n + \alpha_k \delta t G(\mathbf{U}_t^{(k-1)}) \quad (23)$$

$$\mathbf{U}_t^{(k)} = \mathcal{S}(\mathbf{U}_{t^*}^{(k)}) \quad (24)$$

respectively,  $G$  denotes the first term of the right hand side of equation (19) and  $\mathcal{S}$  is a formal iteration operator defined in the following. A Taylor series expansion in time shows that the usual Runge-Kutta scheme of fourth order accuracy  $K = 4$  is obtained for the coefficients  $\alpha_k$  and  $\beta_k$  verifying  $\alpha_1 = 0$ ,  $\alpha_2 = \alpha_3 = 1/2$ ,  $\alpha_4 = 1$ ,  $\beta_1 = \beta_4 = 1/6$ ,  $\beta_2 = \beta_3 = 1/3$  [26]. For comparison purpose, the Runge-Kutta scheme of second-order accuracy  $K = 2$  is also used and obtained for

$\alpha_1 = 0$ ,  $\alpha_2 = 1$ ,  $\beta_1 = \beta_2 = 1/2$ . Secondly, specific numerical schemes are proposed for solving the unsteady equations of the subfilter turbulent energy, subfilter dissipation-rate and subfilter turbulent stresses at each step of the Runge-Kutta scheme including the source terms. From a numerical point of view, the first step consists of solving the redundant equation of the subfilter turbulent energy (11) and equation of the subfilter dissipation-rate (16) that are strongly coupled and, afterwards, to solve the subfilter turbulent stress equation (10) using the preceding values. Figure 1 illustrates the different loops of the numerical temporal procedure for sake of clarity.

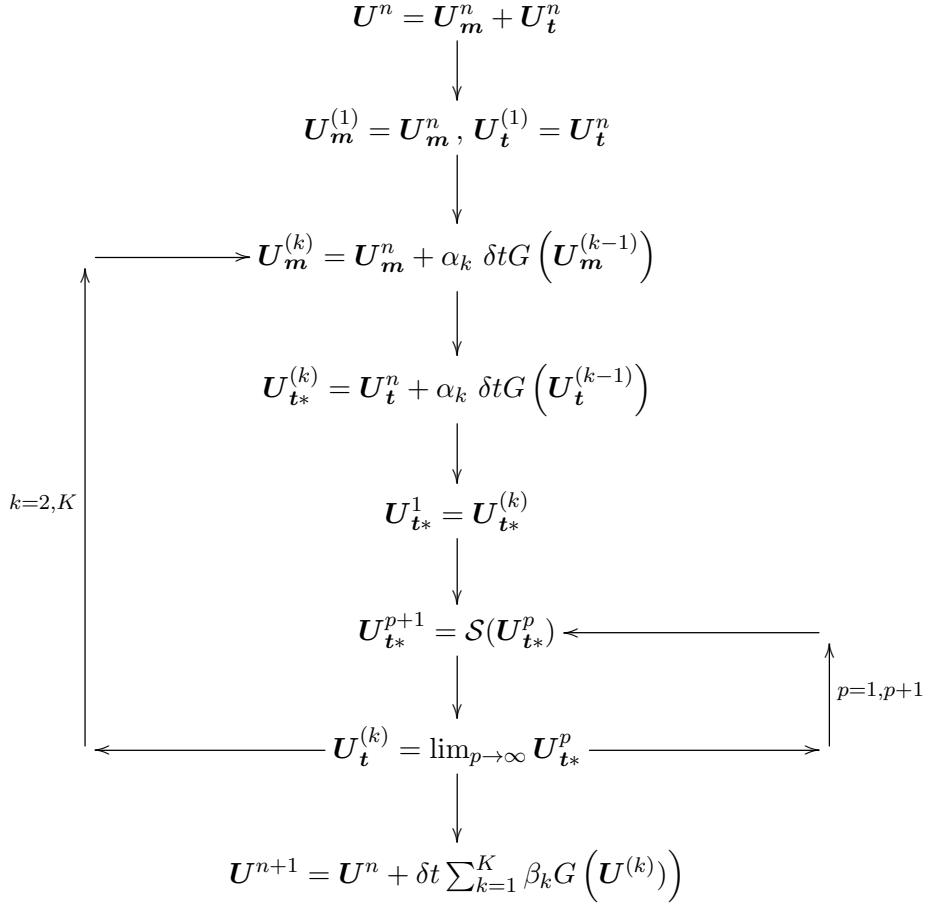


Figure 1 : Schematic of the temporal procedure

Let us consider the step  $(k)$  of the Runge-Kutta method given by equations (22) and (23). The question is to solve the vector  $\mathbf{U}_t^{(k)} = \mathcal{S}(\mathbf{U}_{t*}^{(k)})$ , solution of the turbulent equations governed by the source terms. These equations are discretized implicitly in time by linearizing the source terms as follows

$$\frac{(\bar{\rho}k_{sfs})^{p+1} - (\bar{\rho}k_{sfs})_*^{(k)}}{\alpha_k \delta t} = F_k^p - \left( \frac{\epsilon_{sfs}}{k_{sfs}} \right)^p (\bar{\rho}k_{sfs})^{p+1} \quad (25)$$

and

$$\frac{(\bar{\rho}\epsilon_{sfs})^{p+1} - (\bar{\rho}\epsilon_{sfs})_*^{(k)}}{\alpha_k \delta t} = \left( \frac{\epsilon_{sfs}}{k_{sfs}} \right)^p (c_{\epsilon_1} P_k^p - c_{sfs\epsilon_2} (\bar{\rho}\epsilon_{sfs})^{p+1}) \quad (26)$$

where the turbulent variables are initialized by  $(\bar{\rho}k_{sfs})^1 = (\bar{\rho}k_{sfs})_*^{(k)}$  and  $(\bar{\rho}\epsilon_{sfs})^1 = (\bar{\rho}\epsilon_{sfs})_*^{(k)}$  for  $p = 1$ . When solving equations (25) and (26), one can obtain the solutions  $(\bar{\rho}k_{sfs})^{p+1}$  and  $(\bar{\rho}\epsilon_{sfs})^{p+1}$  that read

$$(\bar{\rho}k_{sfs})^{p+1} = \frac{(\bar{\rho}k_{sfs})_*^{(k)} + P_k^p \alpha_k \delta t}{1 + \left( \frac{\epsilon_{sfs}}{k_{sfs}} \right)^p \alpha_k \delta t} \quad (27)$$

and

$$(\bar{\rho}\epsilon_{sfs})^{p+1} = \frac{(\bar{\rho}\epsilon_{sfs})_*^{(k)} + c_{\epsilon_1} \left( \frac{\epsilon_{sfs}}{k_{sfs}} \right)^p P_k^p \alpha_k \delta t}{1 + c_{sfs\epsilon_2} \left( \frac{\epsilon_{sfs}}{k_{sfs}} \right)^p \alpha_k \delta t} \quad (28)$$

where  $(\bar{\rho}k_{sfs})^{(k)} = \lim_{p \rightarrow \infty} (\bar{\rho}k_{sfs})^p$  and  $(\bar{\rho}\epsilon_{sfs})^{(k)} = \lim_{p \rightarrow \infty} (\bar{\rho}\epsilon_{sfs})^p$ . The discretized stress equation is linearized taking into account the preceding  $(\bar{\rho}k_{sfs})^{p+1}$  and  $(\bar{\rho}\epsilon_{sfs})^{p+1}$  values as follows

$$\begin{aligned} \frac{(\bar{\rho}(\tau_{ij})_{sfs})^{p+1} - (\bar{\rho}(\tau_{ij})_{sfs})_*^{(k)}}{\alpha_k \delta t} &= P_{ij}^p - c_2 \left( P_{ij}^p - \frac{2}{3} P_k^p \delta_{ij} \right) \\ -c_1 \left( \frac{\epsilon_{sfs}}{k_{sfs}} \right)^{p+1} \left( (\bar{\rho}(\tau_{ij})_{sfs})^{p+1} - \frac{2}{3} (\bar{\rho}k_{sfs})^{p+1} \delta_{ij} \right) &- \frac{2}{3} (\bar{\rho}\epsilon_{sfs})^{p+1} \delta_{ij} \end{aligned} \quad (29)$$

In particular, one can see that the Rotta term in this stress equation is discretized by a full implicit formulation. Solving equations (25), (26) and (29) yields the solution  $(\bar{\rho}(\tau_{ij})_{sfs})^{p+1}$

$$(\bar{\rho}(\tau_{ij})_{sfs})^{p+1} = \frac{(\bar{\rho}(\tau_{ij})_{sfs})_*^{(k)} + [P_{ij}^p - c_2 \left( P_{ij}^p - \frac{2}{3} P_k^p \delta_{ij} \right) + \frac{2}{3} (c_1 - 1) (\bar{\rho}\epsilon_{sfs})^{p+1} \delta_{ij}] \alpha_k \delta t}{1 + c_1 \left( \frac{\epsilon_{sfs}}{k_{sfs}} \right)^{p+1} \alpha_k \delta t} \quad (30)$$

When decomposing the productions terms appearing in equation (30) with respect to the stresses and the velocity gradients, the stress  $(\bar{\rho}(\tau_{ij})_{sfs})^{p+1}$  is finally given by

$$(\bar{\rho}(\tau_{ij})_{sfs})^{p+1} = \frac{(\bar{\rho}(\tau_{ij})_{sfs})_*^{(k)} + [t_{ijmn} (\bar{\rho}(\tau_{mn})_{sfs})^p + \frac{2}{3} (c_1 - 1) (\bar{\rho}\epsilon_{sfs})^{p+1} \delta_{ij}] \alpha_k \delta t}{1 + c_1 \left( \frac{\epsilon_{sfs}}{k_{sfs}} \right)^{p+1} \alpha_k \delta t} \quad (31)$$

where  $t_{ijmn}$  denotes a tensorial function of the filtered gradient velocities  $\partial \tilde{u}_i / \partial x_j$  for  $i, j = 1, 2, 3$ . The tensorial components  $t_{ijmn}$  are given in appendix B. At the beginning of the iterations, the stress is initialized by  $(\bar{\rho}(\tau_{ij})_{sfs})^1 = (\bar{\rho}(\tau_{ij})_{sfs})_*^{(k)}$ . The solution of the iterative algorithm is obtained when  $(\bar{\rho}(\tau_{ij})_{sfs})^{(k)} = \lim_{p \rightarrow \infty} (\bar{\rho}(\tau_{ij})_{sfs})^p$ . Obviously, the numerical procedure must also satisfy the trace equality  $(\bar{\rho}k_{sfs})^{(k)} = (\bar{\rho}((\tau_{mm})_{sfs})^{(k)}) / 2$  which is practically verified within two or three internal iterations in practice. The iteration operator  $\mathcal{S}$  appearing in equation (24) is then defined by the algorithms (27), (28), and (31). This numerical procedure is repeated at each step ( $k=1$  to  $K$ )

of the Runge-Kutta method. The stress solution including the diffusion and source contributions is then substituted into the momentum equation (2) allowing the coupling between the mean velocities and subfilter turbulent stresses. Note that these iterative algorithms (27), (28) and (31) are relatively stable because of the denominators that are always greater than unity whatever the  $k_{sfs}$  and  $\epsilon_{sfs}$  values. Still with the aim to improve the numerical scheme stability, it is also useful to average in time the ratio  $T = k_{sfs}/\epsilon_{sfs}$  that appears in the algorithm (28) when performing hybrid RANS/LES simulations because of  $k_{sfs}$  and  $\epsilon_{sfs}$  variables which are more fluctuating in time and space. This time averaging is particularly recommended when the ratio of the subfilter energy to the total energy is very low. This means that the computation progressively goes to quasi DNS (as far as the grid-size is sufficiently refined) [2, 3]. This numerical procedure is also justified from a physical point of view since the ratio  $T = k_{sfs}/\epsilon_{sfs}$  can be viewed as a characteristic time-scale of the turbulence. The averaging can be carried out in the homogeneous directions of the flow and also in time by using the time relaxation such as  $\langle T_f^{n+1} \rangle = \alpha \langle T^{n+1} \rangle + (1 - \alpha) \langle T^n \rangle$  where  $\alpha$  is chosen to 0.5 in the present case. From a numerical point of view, it is now essential to check if the algorithm (31) provides positive values of the normal stresses  $(\tau_{11})_{sfs}$ ,  $(\tau_{22})_{sfs}$  and  $(\tau_{33})_{sfs}$  at each step of the computation. This question is crucial when performing flow simulations. Without losing generality, it is easier from a physical standpoint to examine this question in a coordinate system aligned with the principal axes of the stress tensor. When expressing the tensorial components  $(\tau_{ij})_{sfs}$  from the local coordinate system to the principal coordinate system, the stress  $(\tau_{\alpha\beta})_{sfs} = (\tau_{\alpha\alpha})_{sfs} \delta_{\alpha\beta}$  (no summation on the Greek index) in the principal axes of coordinate is then computed by the tensorial relation  $(\tau_{\alpha\beta})_{sfs} = q_{\alpha l} (\tau_{lm})_{sfs} p_{m\beta}$  where  $p_{ij}$  and  $q_{ij}$  denotes the corresponding transformation tensors verifying  $p_{il} q_{lj} = \delta_{ij}$ . Taking into account the derivative of the tensorial product  $p_{il} q_{lj} = \delta_{ij}$ ,

$$\frac{\partial(q_{il} p_{lj})}{\partial t} = \frac{\partial q_{il}}{\partial t} p_{lj} + q_{il} \frac{\partial p_{lj}}{\partial t} = 0, \quad (32)$$

it is then a straightforward matter to show that the first derivative in time of the stress equation in the principal axes can be written in the mathematical form

$$\frac{\partial}{\partial t} (\bar{\rho} (\tau_{\alpha\beta})_{sfs}) = \gamma_{\alpha k} (\tau_{k\beta})_{sfs} - (\tau_{\alpha n})_{sfs} \gamma_{n\beta} + S_{\alpha\beta} = S_{\alpha\beta} \quad (33)$$

because  $\gamma_{ij} = -q_{il} \partial p_{lj} / \partial t$  and  $(\tau_{ij})_{sfs}$  are an antisymmetric tensor and a symmetric tensor, respectively, implying therefore that the tensor  $\Gamma_{\alpha\beta} = \gamma_{\alpha k} (\tau_{k\beta})_{sfs} - (\tau_{\alpha n})_{sfs} \gamma_{n\beta}$  reduces to zero. The component  $S_{\alpha\beta}$  is given by equation (19). Therefore, the algorithms (27), (28), (30) and (31) remain unchanged and can be applied for computing the stresses in the principal axes of coordinate system. In the aim to conduct the analysis, we assume that at the step  $p$ , the turbulent quantities  $k_{sfs}^p$ ,  $\epsilon_{sfs}^p$ ,  $(\tau_{\alpha\alpha})_{sfs}^p$  have positive values and we prove that at the iteration  $p + 1$ ,  $k_{sfs}^{p+1}$ ,  $\epsilon_{sfs}^{p+1}$  and  $(\tau_{\alpha\alpha})_{sfs}^{p+1}$  are also positive. The algorithm (27) shows that  $k_{sfs}^{p+1}$  is positive if the production term  $P_k^p$  is positive. In this condition, the algorithm (28) also reveals that  $\epsilon_{sfs}^{p+1}$  is positive. The algorithm (30) indicates that  $(\tau_{\alpha\alpha})_{sfs}^{p+1}$  is positive if the quantity

$$N_{\alpha\alpha} = P_{\alpha\alpha}^p - c_2 \left( P_{\alpha\alpha}^p - \frac{2}{3} P_k^p \right) + \frac{2}{3} (c_1 - 1) (\bar{\rho} \epsilon_{sfs})^{p+1} \quad (34)$$

appearing in the numerator is positive. Now, let us analyze the more critical situation which occurs when the stress  $(\tau_{\alpha\alpha})_{sfs}^p$  goes to zero. In this case, one can see that  $P_{\alpha\alpha}^p = -2\bar{\rho}(\tau_{\alpha\alpha})_{sfs}^p \partial\tilde{u}_\alpha/\partial x_\alpha$  goes to zero, so that equation (34) reduces to  $N_{\alpha\alpha} = \frac{2}{3}c_2 P_k^p + \frac{2}{3}(c_1 - 1)(\bar{\rho}\epsilon_{sfs})^{p+1}$  leading to  $c_1 > 1 - c_2 P_k^p / (\bar{\rho}\epsilon_{sfs})^{p+1}$ . This condition corresponds in fact to the weak form of realizability [27]. Due to the expression of the function  $c_1$  that is always greater than unity (see table 1), this constraint is satisfied when the production term of the turbulent energy is positive. In practice, it appears that the algorithms put in place provide positive normal stresses if the subfilter turbulent energy  $k_{sfs}^n$  and the subfilter dissipation-rate  $\epsilon_{sfs}^n$  are previously initialized by a  $k_{sfs} - \epsilon_{sfs}$  computational field. Indeed, for the  $k_{sfs} - \epsilon_{sfs}$  subfilter energy model [1, 28], the production term  $P_k$  remains always positive as a consequence of the Boussinesq hypothesis. When following this numerical procedure, the stresses and dissipation-rate converge towards the solution and no artificial limiter needs to be applied on the stresses during the temporal iterations.

### 3.3 Space discretization

In this section, we propose a numerical scheme in space discretization based on a MUSCL approach and on the use of a weight parameter  $\zeta$  introduced in the slope limiters for performing continuous hybrid non-zonal RANS/LES simulations. In a general way, one has to keep in mind that numerical schemes developed for RANS computations are generally characterized by too high dissipative properties. They cannot be used in LES because they usually smooth the large instantaneous scales. In the present method, the convective flux at the cell interfaces is computed by the approximate Riemann solver as follows [29]

$$\mathbf{F}_{Roe} = \frac{\mathbf{F}(\mathbf{U}^R) + \mathbf{F}(\mathbf{U}^L)}{2} - |\mathbf{J}(\mathbf{U}^R, \mathbf{U}^L)| \left( \frac{\mathbf{U}^R - \mathbf{U}^L}{2} \right) \quad (35)$$

where  $|\mathbf{J}|$  denotes the absolute Jacobian matrix [30] and  $\mathbf{U}^R$  and  $\mathbf{U}^L$  are the right and left states of the fluid at the interface. When developing the calculus, it is found as a result after some algebra that the Jacobian matrix can be expressed as follows

$$\mathbf{J} = \frac{\partial \mathbf{F}}{\partial \mathbf{U}} = \tilde{u}_m n_m \mathbf{I} + c(\mathbf{r}_a \otimes \mathbf{l}^b + \mathbf{r}_b \otimes \mathbf{l}^a) \quad (36)$$

where in this expression,  $\mathbf{I}$  is the identity matrix,  $\mathbf{r}_a$  and  $\mathbf{r}_b$  are two vectors whereas  $\mathbf{l}^a$  and  $\mathbf{l}^b$  denote two row vectors. At this step, we introduce the vectors  $\mathbf{r}_+$ ,  $\mathbf{r}_-$  and  $\mathbf{l}^+$ ,  $\mathbf{l}^-$  defined by  $\mathbf{r}_+ = \mathbf{r}_a + \mathbf{r}_b$ ,  $\mathbf{r}_- = \mathbf{r}_a - \mathbf{r}_b$ ,  $\mathbf{l}^+ = (\mathbf{l}^a + \mathbf{l}^b)/2$  and  $\mathbf{l}^- = (\mathbf{l}^a - \mathbf{l}^b)/2$ , and we demonstrate that they are the right and left eigenvectors of the Jacobian matrix  $\mathbf{J}$  with the eigenvalues  $\lambda^+ = \tilde{u}_m n_m + c$ ,  $\lambda^- = \tilde{u}_m n_m - c$ ,  $\lambda^0 = \tilde{u}_m n_m$  involving the acoustic and convective modes, respectively, where  $c$  is the velocity of sound (see appendix C). Equation (36) can be rewritten in the base of the eigenvectors under a spectral decomposition form as (see appendix D)

$$\mathbf{J} = \lambda^0 (\mathbf{I} - \mathbf{r}_+ \otimes \mathbf{l}^+ - \mathbf{r}_- \otimes \mathbf{l}^-) + \lambda^+ (\mathbf{r}_+ \otimes \mathbf{l}^+) + \lambda^- (\mathbf{r}_- \otimes \mathbf{l}^-) \quad (37)$$

and due to its definition, although being of complex expression, the absolute Jacobian matrix is then obtained by

$$|\mathbf{J}| = |\lambda^0| \mathbf{I} + [|\lambda^+| - |\lambda^0|] \mathbf{r}_+ \otimes \mathbf{l}^+ + [|\lambda^-| - |\lambda^0|] \mathbf{r}_- \otimes \mathbf{l}^- \quad (38)$$

The function  $|\mathbf{J}|(\mathbf{U}^R - \mathbf{U}^L)$  is then determined by means of equation (38) by

$$|J_{im}|(U_m^R - U_m^L) = |\lambda^0|(U_i^R - U_i^L) + [|\lambda^+| - |\lambda^0|] r_{+i} [l_m^+(U_m^R - U_m^L)] + [|\lambda^-| - |\lambda^0|] r_{-i} [l_m^-(U_m^R - U_m^L)] \quad (39)$$

Equation (38) is of the same form as equation derived by Dutoya and Errera [31] for the Euler equations but the vectors  $\mathbf{r}_+$ ,  $\mathbf{r}_-$ ,  $\mathbf{l}^+$  and  $\mathbf{l}^-$  take a more complex expressions because of the convection of the turbulent variables  $(\tau_{ij})_{sfs}$  and  $\epsilon_{sfs}$ . It can be noted that the presence of the subfilter turbulent stress in the pressure equation (9) suggests a strong coupling between the mean equations and the turbulent transport equations. Since the absolute Jacobian matrix  $|\mathbf{J}|$  is not explicitly computed in equation (35), but only its function  $|\mathbf{J}|(\mathbf{U}^R - \mathbf{U}^L)$  involving the scalar products  $l_m^+(U_m^R - U_m^L)$  and  $l_m^-(U_m^R - U_m^L)$ , and that  $\lambda_0$  is a degenerate eigenvalue of order  $n - 2$ , this method allows to reduce the computational cost in comparison with conventional algorithms. More precisely, the computation of the Jacobian function of dimension  $n \times n$  where  $n = 12$ , using equation (39), requires  $9n + 2$  flops ( $4n$  additions:  $2n$  per line and  $2n$  per column and  $5n + 2$  multiplications:  $2n + 2$  per line and  $3n$  per column) instead of  $2n^2 - n$  flops ( $n^2 - n$  additions and  $n^2$  multiplications) for a conventional matrix algorithm where  $|J_{im}|$  is explicitly computed. Moreover, this numerical procedure can be easily implemented in computational codes with a high degree of vectorization because of the basic form of the Jacobian function. The evaluation of the flux defined by equation (35) requires the knowledge of the right and left states  $\mathbf{U}^R$  and  $\mathbf{U}^L$  of the fluid at the grid interface. They are calculated by a MUSCL approach using five computational points. The variables  $\mathbf{U}_{i+\frac{1}{2},j,k}^L$  and  $\mathbf{U}_{i+\frac{1}{2},j,k}^R$  at the left and right sides of the interface  $(i + \frac{1}{2}, j, k)$  are defined by means of the relations

$$\mathbf{U}_{i+\frac{1}{2},j,k}^L = \Phi_{i+\frac{1}{2},j,k}^L \mathbf{U}_{i+\frac{1}{2},j,k}^{L*} + (1 - \Phi_{i+\frac{1}{2},j,k}^L) \mathbf{U}_{i+\frac{1}{2},j,k}^C \quad (40)$$

and

$$\mathbf{U}_{i+\frac{1}{2},j,k}^R = \Phi_{i+\frac{1}{2},j,k}^R \mathbf{U}_{i+\frac{1}{2},j,k}^{R*} + (1 - \Phi_{i+\frac{1}{2},j,k}^R) \mathbf{U}_{i+\frac{1}{2},j,k}^C \quad (41)$$

where the variables  $\mathbf{U}_{i+\frac{1}{2},j,k}^{L*}$  and  $\mathbf{U}_{i+\frac{1}{2},j,k}^{R*}$  are evaluated by interpolation of the variables  $\mathbf{U}_{i-1,j,k}$ ,  $\mathbf{U}_{i,j,k}$ ,  $\mathbf{U}_{i+1,j,k}$  and  $\mathbf{U}_{i+2,j,k}$  by a Taylor series expansion in space

$$\mathbf{U}_{i+\frac{1}{2},j,k}^{L*} = \frac{-\Delta x_{i,j,k} \mathbf{U}_{i-1,j,k} + (\Delta x_{i-1,j,k} + 2\Delta x_{i,j,k}) \mathbf{U}_{i,j,k}}{\Delta x_{i-1,j,k} + \Delta x_{i,j,k}}, \quad (42)$$

$$\mathbf{U}_{i+\frac{1}{2},j,k}^{R*} = \frac{(2\Delta x_{i+1,j,k} + \Delta x_{i+2,j,k}) \mathbf{U}_{i+1,j,k} - \Delta x_{i+1,j,k} \mathbf{U}_{i+2,j,k}}{\Delta x_{i+1,j,k} + \Delta x_{i+2,j,k}} \quad (43)$$

whereas the centered variable  $\mathbf{U}_{i+\frac{1}{2},j,k}^C$  is computed by a symmetric interpolation of the variables  $\mathbf{U}_{i,j,k}$  and  $\mathbf{U}_{i+1,j,k}$

$$\mathbf{U}_{i+\frac{1}{2},j,k}^C = \frac{\Delta x_{i+1,j,k} \mathbf{U}_{i,j,k} + \Delta x_{i,j,k} \mathbf{U}_{i+1,j,k}}{\Delta x_{i,j,k} + \Delta x_{i+1,j,k}} \quad (44)$$

In equations (40) and (41), the quantities  $\Phi_{i+\frac{1}{2},j,k}^L$  and  $\Phi_{i+\frac{1}{2},j,k}^R$  denote the slope limiters which are defined by

$$\Phi_{i+\frac{1}{2},j,k}^L = \frac{\zeta x_A^L |\mathbf{U}_{i+1,j,k} - \mathbf{U}_{i,j,k}|}{x_A^L |\mathbf{U}_{i+1,j,k} - \mathbf{U}_{i,j,k}| + x_B^L |\mathbf{U}_{i,j,k} - \mathbf{U}_{i-1,j,k}|}, \quad (45)$$

$$\Phi_{i+\frac{1}{2},j,k}^R = \frac{\zeta x_A^R |U_{i+1,j,k} - U_{i,j,k}|}{x_A^R |U_{i+1,j,k} - U_{i,j,k}| + x_B^R |U_{i+2,j,k} - U_{i+1,j,k}|} \quad (46)$$

with the definitions

$$x_A^L = \frac{\Delta x_{i,j,k}}{\Delta x_{i,j,k} + \Delta x_{i+1,j,k}}, \quad (47)$$

$$x_B^L = \frac{\Delta x_{i,j,k}}{\Delta x_{i-1,j,k} + \Delta x_{i,j,k}}, \quad (48)$$

$$x_A^R = \frac{\Delta x_{i+1,j,k}}{\Delta x_{i,j,k} + \Delta x_{i+1,j,k}}, \quad (49)$$

$$x_B^R = \frac{\Delta x_{i+1,j,k}}{\Delta x_{i+1,j,k} + \Delta x_{i+2,j,k}} \quad (50)$$

and where the quantity  $\Delta x_{i,j,k} = x_1(i + \frac{1}{2}, j, k) - x_1(i - \frac{1}{2}, j, k)$  denotes the spatial increment of the grid size and  $\zeta$  is a parameter coefficient introduced in equations (45) and (46). The slope limiters satisfy the limiting conditions :

- (i) if  $U_{i-1,j,k} = U_{i,j,k} \Rightarrow \Phi_{i+\frac{1}{2},j,k}^L = 1 \Rightarrow U_{i+\frac{1}{2},j,k}^L = U_{i+\frac{1}{2},j,k}^{L*}$ ,
- (ii) if  $U_{i,j,k} = U_{i+1,j,k} \Rightarrow \Phi_{i+\frac{1}{2},j,k}^L = 0, \Phi_{i+\frac{1}{2},j,k}^R = 0 \Rightarrow U_{i+\frac{1}{2},j,k}^L = U_{i+\frac{1}{2},j,k}^C, U_{i+\frac{1}{2},j,k}^R = U_{i+\frac{1}{2},j,k}^C$ ,
- (iii) if  $U_{i+1,j,k} = U_{i+2,j,k} \Rightarrow \Phi_{i+\frac{1}{2},j,k}^R = 1 \Rightarrow U_{i+\frac{1}{2},j,k}^R = U_{i+\frac{1}{2},j,k}^{R*}$ .

It is straightforward matter to show that the slope limiter with  $\zeta = 1$  defined in equations (45) and (46) corresponds to the Van Leer's limiter in the Sweby diagram [32, 26]. As it will be show in the following, the vector of the mean variables  $\mathbf{U}_m = \bar{\rho} [1, \tilde{u}_1, \tilde{u}_2, \tilde{u}_3, \tilde{E}]^T$  can be computed by a centered scheme in space discretization if associated with a fourth-order Runge-Kutta scheme in time or by a weighted scheme of more or less centered formulation where  $\zeta \ll 1$  but not equal to zero if associated to a lower time accurate scheme for suppressing the spurious oscillations and discontinuities produced by a purely space centered scheme. On the contrary, the vector of the turbulent variables  $\mathbf{U}_t = \bar{\rho} [(\tau_{11})_{sfs}, (\tau_{12})_{sfs}, (\tau_{13})_{sfs}, (\tau_{22})_{sfs}, (\tau_{23})_{sfs}, (\tau_{33})_{sfs}, \epsilon_{sfs}]^T$  is computed by a more or less upwind scheme obtained for  $\zeta = 1$ , depending on the slope limiters  $\Phi$  that are activated in presence of discontinuities. As usual, the viscous fluxes are computed using a second-order accurate scheme in space discretization.

### 3.4 Analysis of the numerical scheme diffusion

In this section, we analyze the numerical scheme diffusion in order to characterize the slope limiters effects. Since the analysis cannot be conducted analytically when applying high-order Runge-Kutta schemes, an exact numerical scheme in time is assumed in a first step for providing qualitative results. The analysis is worked out for linear hyperbolic problems by means of the formulation of the equivalent differential equation [33]. Therefore, we consider the acoustic equation

$$\frac{\partial u}{\partial t} + c \frac{\partial u}{\partial x} = 0 \quad (51)$$

and we applied the numerical scheme in space discretization defined in the preceding section. In this case, equation (51) is solved by the semi-discretized equation

$$\frac{\partial u}{\partial t} + c \left[ (1 - \Phi) \frac{u_{i+1} - u_{i-1}}{2\Delta_x} + \Phi \frac{3u_i - 4u_{i-1} + u_{i-2}}{2\Delta_x} \right] = 0 \quad (52)$$

The equivalent differential equation is then constructed by introducing the Taylor series expansion in space of the velocity in equation (52) and one can obtain

$$\frac{\partial u}{\partial t} + c \frac{\partial u}{\partial x} = -a_3 \frac{\partial^3 u}{\partial x^3} - a_4 \frac{\partial^4 u}{\partial x^4} + O(\Delta_x^4) \quad (53)$$

where the coefficients  $a_3$  and  $a_4$  are defined by  $a_3 = c(1 - 3\Phi)\Delta_x^2/6$  and  $a_4 = c\Phi\Delta_x^3/2$ . A solution of equation (53) can be searched in the basic form such as  $u = u_0 e^{j\kappa x} \xi(t)$  where  $u_0$  is a constant coefficient whereas  $\xi$  is a function which needs to be determined. It is then straightforward matter to show that  $\xi$  must verify the differential equation

$$\frac{\partial \xi}{\partial t} + [j(c\kappa - a_3\kappa^3) + a_4\kappa^4] \xi = 0 \quad (54)$$

leading to the final solution in time and space as follows

$$u(x, t) = u_0 e^{j\kappa(x-ct)} e^{ja_3\kappa^3 t} e^{-a_4\kappa^4 t} \quad (55)$$

Equation (55) clearly shows that the diffusion including the dispersion and dissipation processes depends linearly on the slope limiter and on the velocity of sound and is a function of the quadratic and cubic grid spacings. The numerical dissipation is proportional to the velocity of sound and varies in  $a_4\kappa^4$  law with respect to the wave number. The ratio of the real to the theoretical propagation speed is given by  $r = 1 - (a_3/c)\kappa^2$  showing that it is a decreasing quadratic function of the wave number. The propagation velocity is equal to zero for  $\kappa_c = \sqrt{c/a_3}$ . When applying high-order Runge-Kutta schemes, the analysis cannot be conducted theoretically because of the increased mathematical complexity arising from the equations [34]. These results are changed with respect to the time accuracy of the scheme but the analysis still shows the importance influence of the space discretization in the solution.

## 4 Flow test cases

### 4.1 Decay of isotropic spectrum

In the following, we simulate the decay of homogeneous spectrum by using the subfilter stress model and the second and fourth-order Runge-Kutta schemes for comparison purposes. Indeed, isotropic decaying turbulence serves an important benchmark for studying the energy transfer capability of subfilter stress models [35, 36]. We consider different values of the coefficient  $\zeta$  appearing in the slope limiters (45) and (46) for evaluating its effects on the numerical results. The initial mean

velocity is zero and an analytical homogeneous random field [37] has been generated in a cubic box of size  $L = N\Delta$  as initial condition with a given energy spectrum verifying

$$\langle \hat{u}_i(\boldsymbol{\kappa}) \hat{u}_i(-\boldsymbol{\kappa}) \rangle = \left( \frac{2\pi}{L} \right)^3 \frac{E(\kappa)}{2\pi\kappa^2} \quad (56)$$

where  $\hat{u}_i(\boldsymbol{\kappa})$  denotes the Fourier transform of the velocity. The wave-numbers are defined by  $\boldsymbol{\kappa} = 2\pi [m, n, p]^T / L$  where  $m, n, p$  are integers that vary from  $-N/2 + 1$  to  $N/2$  leading to a minimum wave-number  $\kappa_{min} = 2\pi / (N\Delta)$  and a maximum wave-number  $\kappa_{max} = \pi / \Delta$ . The energy spectrum is defined by

$$\begin{aligned} E(\kappa) &= \beta \kappa^m \quad \text{for } \kappa \leq \kappa_0 \\ E(\kappa) &= C_\kappa \epsilon^{2/3} \kappa^{-5/3} \quad \text{for } \kappa \geq \kappa_0 \end{aligned} \quad (57)$$

where  $C_\kappa$  is the Kolmogorov constant. The maximum of the spectrum is obtained for  $\kappa_0$  which is defined by the continuity of the two functions in equation (57)

$$\kappa_0 = \left( \frac{C_\kappa \epsilon^{2/3}}{\beta} \right)^{\frac{3}{3m+5}} \quad (58)$$

The subfilter and resolved parts of the energy are determined by integration of the spectrum. For  $\kappa_c > \kappa_0$ , the subfilter energy is given by

$$k_{sfs} = \int_{\kappa_c}^{\infty} E(\kappa) d\kappa = \frac{3}{2} C_\kappa \epsilon^{2/3} \kappa_c^{-2/3} \quad (59)$$

whereas the total energy is

$$k = \int_0^{\infty} E(\kappa) d\kappa = \frac{3m+5}{2(m+1)} C_\kappa \epsilon^{2/3} \kappa_0^{-2/3} = \frac{3m+5}{2(m+1)} \beta^{\frac{2}{3m+5}} C_\kappa^{\frac{3(m+1)}{3m+5}} \epsilon^{\frac{2(m+1)}{3m+5}} \quad (60)$$

leading to the ratio of the subfilter energy to the total energy

$$\frac{k_{sfs}}{k} = \frac{3(m+1)}{3m+5} \left( \frac{\kappa_0}{\kappa_c} \right)^{2/3} \quad (61)$$

The simulations are performed on the same grid  $N = 80^3$  for a medium cutoff wave number  $\kappa_c = 3\kappa_{max}/4 \approx 3\kappa_0$ . The equation describing the law of the dissipation-rate decay can be easily obtained by taking the derivative of equation (60)

$$\frac{dk}{k} = \left( \frac{2m+2}{3m+5} \right) \frac{d\epsilon}{\epsilon} \quad (62)$$

and by considering the equation of the turbulent energy decay,

$$\frac{dk}{dt} = -\epsilon, \quad (63)$$

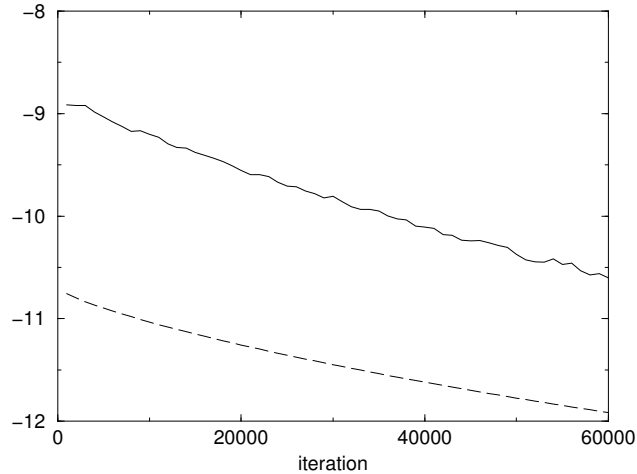


Figure 2: Residual profiles of the turbulent variables —  $\rho(\tau_{11})_{sfs}$ ; - -  $\rho\epsilon_{sfs}$ .

one can finally obtain the resulting equation

$$\frac{d\epsilon}{dt} = - \left( \frac{3m+5}{2m+2} \right) \frac{\epsilon^2}{k} \quad (64)$$

For the particular value  $m = 1.4$ , the present limiting value  $\lim_{\eta_c \rightarrow 0} c_{sfs\epsilon_2}(\eta_c) = c_{\epsilon_2} \approx 1.9$  is recovered [1, 5]. The turbulent Reynolds number  $R_t = k^2/\nu\epsilon$  based on the turbulent energy and the dissipation-rate is about 800. For this case, the ratio value of the subfilter energy to the total energy is roughly 0.36 implying an appreciable part of subfilter turbulence energy. The simulations are performed for different values of the coefficient  $\zeta$  and the results are plotted for  $\zeta = 0$ ,  $\zeta = 3 \cdot 10^{-3}$  and  $\zeta = 1$ . Figure 2 shows the variation rate

$$R = \log \sqrt{\frac{1}{N} \sum_{i,j,k} \left( \frac{u_{i,j,k}^{n+1} - u_{i,j,k}^n}{u_{i,j,k}^n} \right)^2} \quad (65)$$

for the turbulent variables  $\rho(\tau_{11})_{sfs}$  and  $\rho\epsilon_{sfs}$ . One can observe that the residual profiles decrease regularly with respect to the temporal iterations indicating that the numerical solver is perfectly stable. Figure 3 shows the  $Q$  isosurfaces [38] of the turbulent flowfield. Although the grid  $80^3$  is not sufficiently refined to provide a realistic description of the flow structures, one can see however the existence of vortical structures called fine scale worms. This figure can be qualitatively compared with figure 3 of reference [36] which is of better resolution  $128^3$ , showing the iso-vorticity surfaces. Figures 4 and 5 display the decay of the three-dimensional spectra starting from the initial time, corresponding to different values of the coefficient  $\zeta$  and different Runge-Kutta schemes. It is found that the fourth-order Runge-Kutta scheme associated with the spatial scheme with the parameter  $\zeta = 0$  and  $\zeta = 3 \cdot 10^{-3}$  produces a decay of the energy spectrum according to the Kolmogorov  $\kappa^{-5/3}$  law even if for  $\zeta = 0$ , one can remark that the spectrum is however marked by a very slight

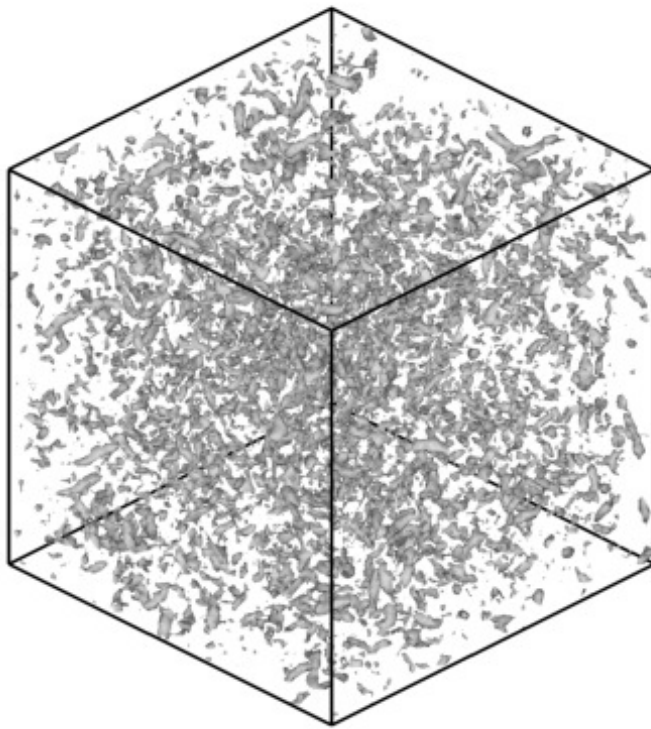


Figure 3: Vortical activity in isotropic homogeneous turbulence illustrated by the  $Q$  isosurfaces. PITM simulation  $80^3$ .

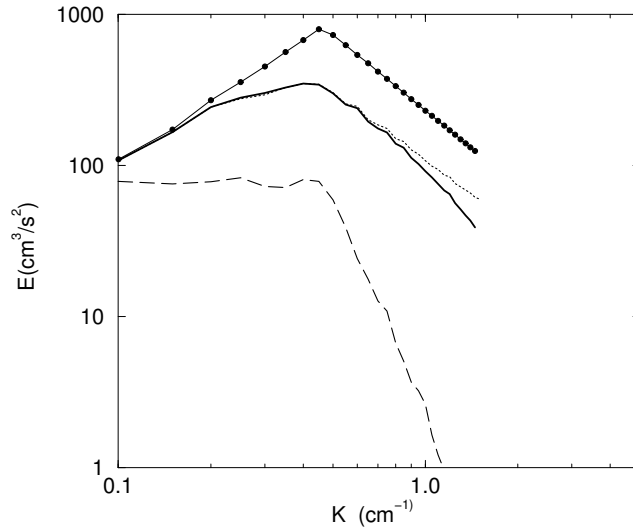


Figure 4: Homogeneous decay of the energy spectra using the fourth-order Runge-Kutta method.  $\kappa_c = 3\kappa_{max}/4 = 1.5 \text{ cm}^{-1}$ . • Initial spectrum given by equation (57);  $\cdots$   $\zeta = 0$ ;  $—$   $\zeta = 3 \cdot 10^{-3}$ ;  $- -$   $\zeta = 1$ .

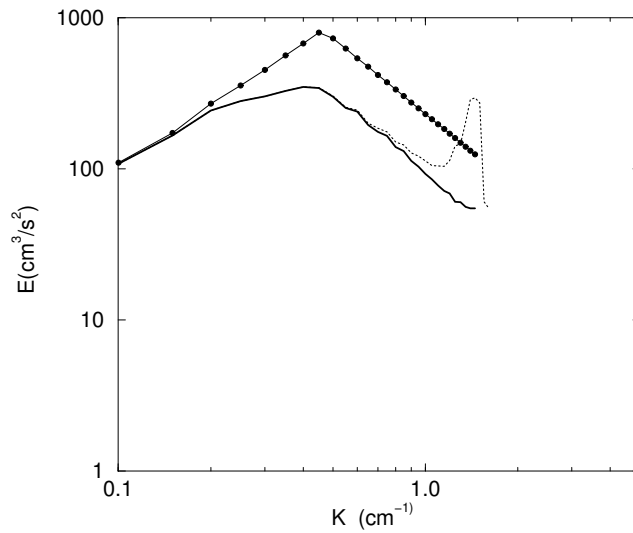


Figure 5: Homogeneous decay of the energy spectra using the second-order Runge-Kutta method.  $\kappa_c = 3\kappa_{max}/4 = 1.5 \text{ cm}^{-1}$ . • Initial spectrum given by equation (57);  $\cdots$   $\zeta = 0$ ;  $—$   $\zeta = 3 \cdot 10^{-3}$ ;

reincrease of the energy in the inertial zone. As expected, the numerical scheme defined with  $\zeta = 1$  yields an erroneous spectrum due to too high dissipation. This result clearly indicates that the space integration has a major impact on the numerical dissipation. The present combination of the fourth-order Runge-Kutta scheme with a centered or a quasi-centered scheme in space discretization appears well appropriate, the small scales and afterwards, the large scales being dissipated by the turbulence model. On the other hand, the second-order Runge-Kutta scheme associated with a purely centered spatial scheme ( $\zeta = 0$ ) yields a spectrum characterized by a strong non-physical rise of energy that appears for high wave numbers in the cutoff wave region, suggesting an accumulation of energy in the box. In the present case, this is a numerical problem caused by the combination of a low order accuracy scheme in time with a purely centered scheme in space discretization that has the effect to produce non-physical oscillations. Note that the role of the turbulence model is to dissipate the small scales of turbulent energy and not spurious oscillations. One can attempt to explain this result by analyzing the numerical scheme properties. As it was shown in the preceding section, the numerical scheme dispersion is governed by the function  $a_3/c = 1 - (1 - 3\Phi)(\kappa \Delta x)^2/6$ . For a centered scheme corresponding to  $\Phi = 0$ , this function decreases to zero with respect to the wave number implying that the propagation velocity goes to zero. So that, the “bump” of energy is mainly due to the dispersive behavior of the centered scheme that injects energy at the small scales, altering the kinetic energy spectrum. The second order Runge-Kutta scheme associated with the spatial scheme with the parameter  $\zeta = 3 \cdot 10^{-3}$  is able to correctly reproduce the evolution of the spectrum in accordance with the Kolmogorov law except however in the immediate vicinity of the cutoff wave number region. In practice, the second order Runge-Kutta scheme can be used for performing LES simulations of aerodynamic flows encountered in engineering applications subjected to complex physical processes such as for instance strong effects of streamline curvature, system rotation, adverse pressure gradients, shock waves, with a reduction of the computational cost. In this case, the coefficient  $\zeta$  can be slightly adjusted for efficiently suppressing non-physical oscillations produced by a purely centered scheme. In order to remove any spurious mode problem, only the fourth-order Runge-Kutta scheme will be applied in the following calculations.

## 4.2 Fully turbulent channel flow

The numerical solver is tested on the well known fully turbulent channel flow. Different grids are generated with coarse and medium resolutions  $16 \times 32 \times 64$  and  $32 \times 64 \times 84$ , respectively in the streamwise, spanwise and normal directions  $(x_1, x_2, x_3)$  for checking the grid independence of the solutions. A minimal size of the box has been retained  $2\delta \times 2\delta \times \delta$  but it is sufficient for ensuring the vanishing of two-point correlation functions in the streamwise direction [2]. In the normal direction to the wall, the grid points are distributed using non-uniform spacing with refinement near the wall whereas they are uniform in the two remaining directions,  $\Delta_1^+ = 105.3$ ,  $\Delta_2^+ = 50.9$  for case 1 and  $\Delta_1^+ = 50.9$ ,  $\Delta_2^+ = 25.1$  for case 2. The PITM results are compared with DNS performed by Moser et al. [39] for a Reynolds number  $R_\tau = 395$ , based on the friction velocity  $u_\tau$  and the channel half width  $\delta/2$ . Figure 6 shows the profiles of the statistical mean velocity  $\langle u_1 \rangle / u_\tau$  for the PITM simulations performed on the coarse grid  $16 \times 32 \times 64$  and on the medium grid  $32 \times 64 \times 84$ , respectively. It can be seen that the mean velocity profiles agree very well with the DNS data [39]. Figure 7 and 8 display the evolutions of the normalized stresses computed as

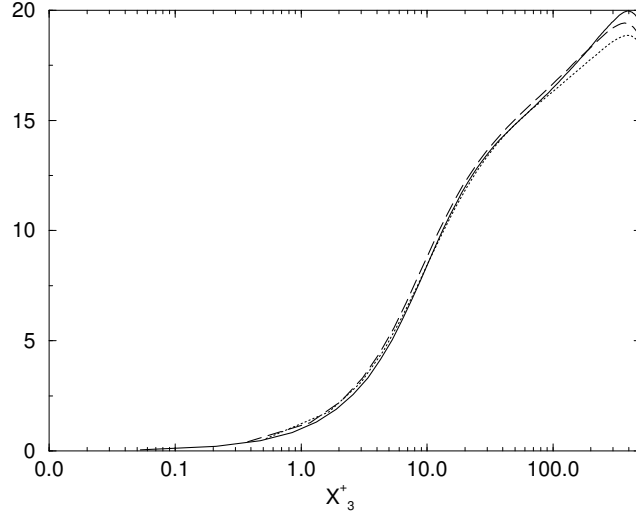


Figure 6: Mean velocity profile;  $\langle u_1 \rangle / u_\tau$  PITM 1 ( $16 \times 32 \times 64$ ) ...; PITM 2 ( $32 \times 64 \times 84$ ) - -; DNS —;  $R_\tau = 395$ .

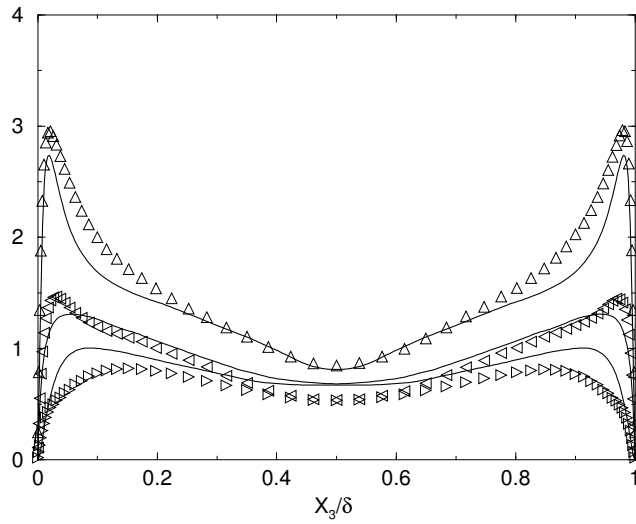


Figure 7: Turbulent Reynolds stresses  $\tau_{ii}^{1/2} / u_\tau$ . ( $16 \times 32 \times 64$ ). PITM1:  $\triangle$ :  $i=1$ ;  $\triangleleft$ :  $i=2$ ;  $\triangleright$ :  $i=3$ ; DNS —;  $R_\tau = 395$ .

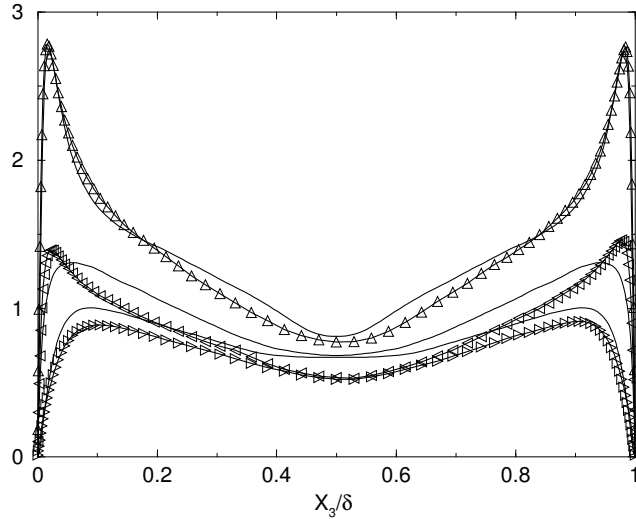


Figure 8: Turbulent Reynolds stresses  $\tau_{ii}^{1/2}/u_\tau$ . ( $32 \times 64 \times 84$ ). PITM2:  $\triangle$ :  $i=1$ ;  $\triangleleft$ :  $i=2$ ;  $\triangleright$ :  $i=3$ ; DNS  $:-$ ;  $R_\tau = 395$ .

the sum of the subfilter and resolved parts  $\tau_{ii}^{1/2}/u_\tau = (\langle(\tau_{ii})_{sfs}\rangle + \langle(\tau_{ii})_{les}\rangle)^{1/2}/u_\tau$  for both PITM simulations. As a result, it appears that both PITM simulations return turbulent stresses in a good agreement with the DNS data. The flow anisotropy is well reproduced by both simulations but the turbulent peak predicted by the PITM1 simulation performed on the coarse grid is slightly overpredicted in comparison with the reference data.

### 4.3 Turbulent channel flow over periodic hills

In this section, we simulate the case of the periodic flow over a 2D hill for illustrating the potential of the numerical solver in presence of curvilinear geometry. This case constitutes a challenging test in aerodynamics because of the turbulence mechanisms associated with separation, recirculation, reattachment, acceleration and wall flow effects that are difficult to reproduce numerically. Concerning the geometry, the hill constricts the channel by about one third of its height and are spaced at a distance of about 9 hill heights denoted  $h$ . According to previous studies conducted by means of the two-point correlation function [40, 41], the dimension in the spanwise direction is fixed to  $4.5 h$ . The Reynolds number, based on the hill height and the bulk velocity about the crest is 10595. In the present case, the flow is performed on a very coarse grid  $80 \times 30 \times 100$  of  $2.4 \cdot 10^5$  grid-points and on a medium grid  $160 \times 60 \times 100$  of  $9.6 \cdot 10^5$  grid points in the streamwise, spanwise and normal directions, respectively, and the results are compared with the data of the highly resolved LES performed on a refined grid of  $13.1 \cdot 10^6$  grid-points by Breuer et al. [41] using the dynamic Smagorinsky model. The coarse grid is deliberately chosen to highlight the ability of the PITM method to simulate large scales of the flow. The medium grid is considered for investigating the effects of the grid refinement on the solution. This choice is motivated by the study of the consistency of the subfilter model when the filter width is changed. In regard with highly

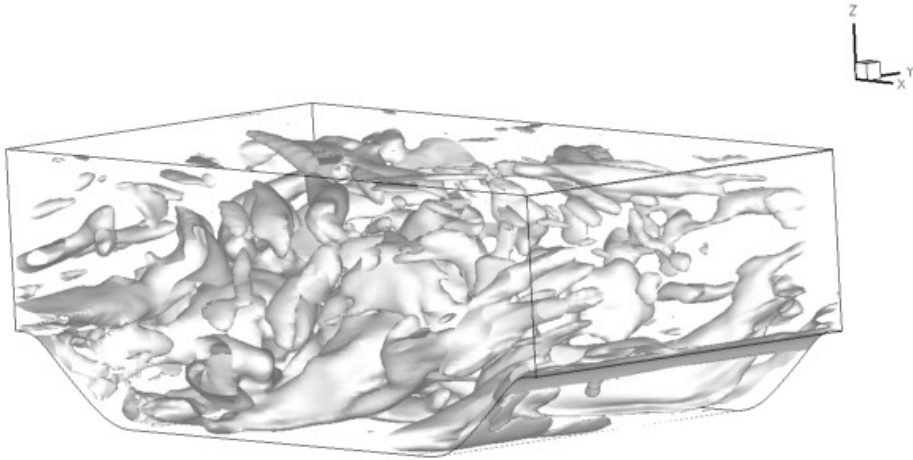


Figure 9: Vortical activity illustrated by the  $Q$  isosurfaces. PITM2 simulation  $160 \times 60 \times 100$ .

resolved LES simulations which require that the spectral cutoff wavenumber is located within the inertial range, PITM simulations can be performed on meshes of different grid resolutions since the cutoff wavenumber can be located almost anywhere within the spectrum [1, 2, 4, 3]. The present grids are refined in the lower and upper wall regions. One can notice that the use of the subfilter stress model derived by the PITM method (see appendix A) allows to considerably reduce the number of grid points. The flow is periodic in the streamwise and spanwise directions so that it removes the need to specify the inflow conditions. Figure 9 shows the  $Q$  isosurfaces computed on the medium grid  $160 \times 60 \times 100$  by the PITM2 simulation. This figure reveals the presence of elongated structures that clearly illustrate the three dimensional nature of the flow although the geometry is two-dimensional. Obviously, the grid resolution is not sufficient in the streamwise and spanwise directions to get a fine description of these structures and a more quantitative structural information requires DNS resolutions. Figure 10 displays the streamlines of the instantaneous flowfield in the mid-plane of the channel for both PITM simulations. One can remark that the large turbulent eddies computed on the coarse grid  $80 \times 30 \times 100$  by the PITM1 simulation are relatively weak and smoothing varying whereas those computed on the medium grid  $160 \times 60 \times 100$  by the PITM2 simulation are more evolving in space. Figure 11 shows the streamlines of the average flowfield for both PITM simulations. The recirculation zone that extends in the lower wall region is well visible. One can see that the flow statistically separates at  $x_1/h \approx 0.23$  downstream the hill crest and reattaches at  $x_1/h \approx 4.3$ . Figure 12 describes the evolution of the friction coefficient along the lower wall computed by both PITM simulations. The friction coefficient first decreases in the entrance of the channel, and afterwards increases toward zero at the reattachment point that occurs at  $x/h \approx 4.3$ . These evolutions present a very good agreement with the data of highly resolved LES performed by Breuer et al. [41] even if some discrepancies attributed to

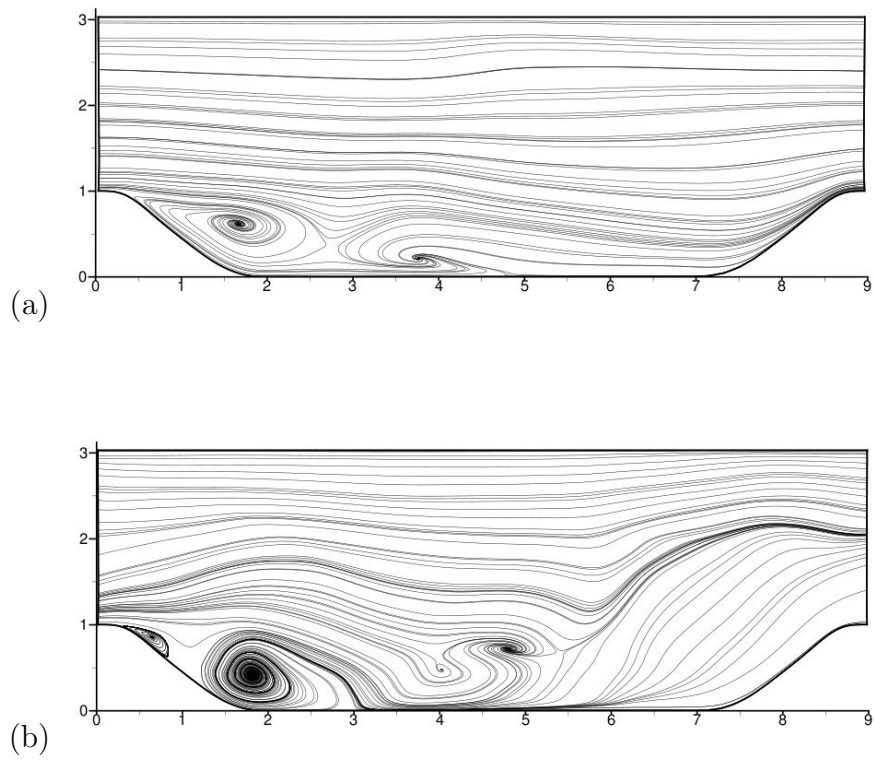


Figure 10. Streamlines of the instantaneous flowfield in the mid-plane of the channel at  $x_2/h = 2$ . (a) PITM1 simulation ( $80 \times 30 \times 100$ ). (b) PITM2 simulation ( $160 \times 60 \times 100$ ).

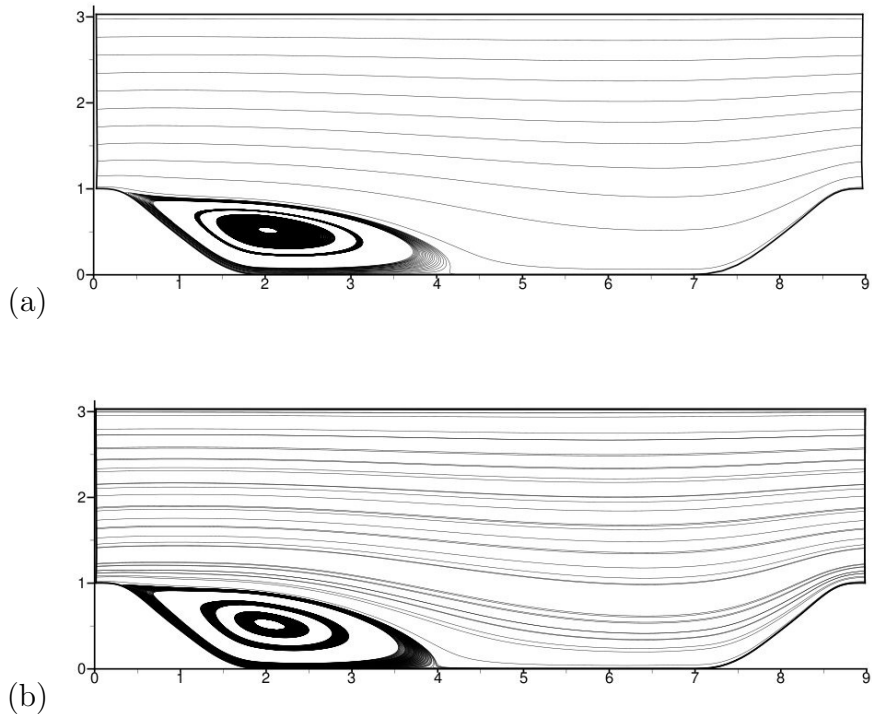


Figure 11. Streamlines of the average flowfield. (a) PITM1 simulation ( $80 \times 30 \times 100$ ). (b) PITM2 simulation ( $160 \times 60 \times 100$ ).

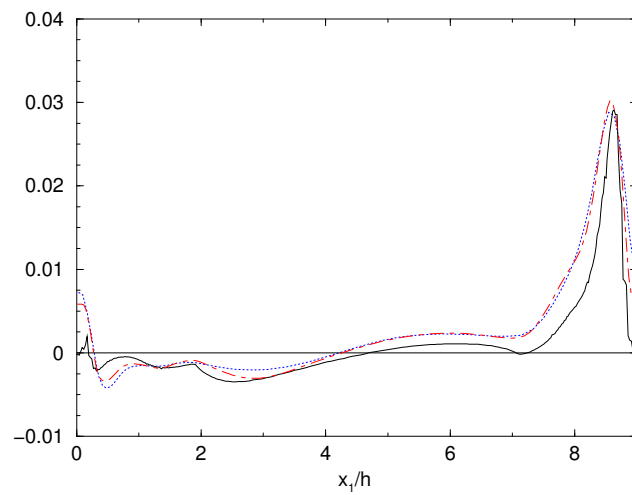


Figure 12: Friction coefficient  $C_f = \tau_w / (0.5 \rho U_b^2)$  along the lower wall LES (Breuer *et al.*, 2009) —; PITM1 ( $80 \times 30 \times 100$ )  $\cdots$ ; PITM2 ( $160 \times 60 \times 100$ ); -.-.-.

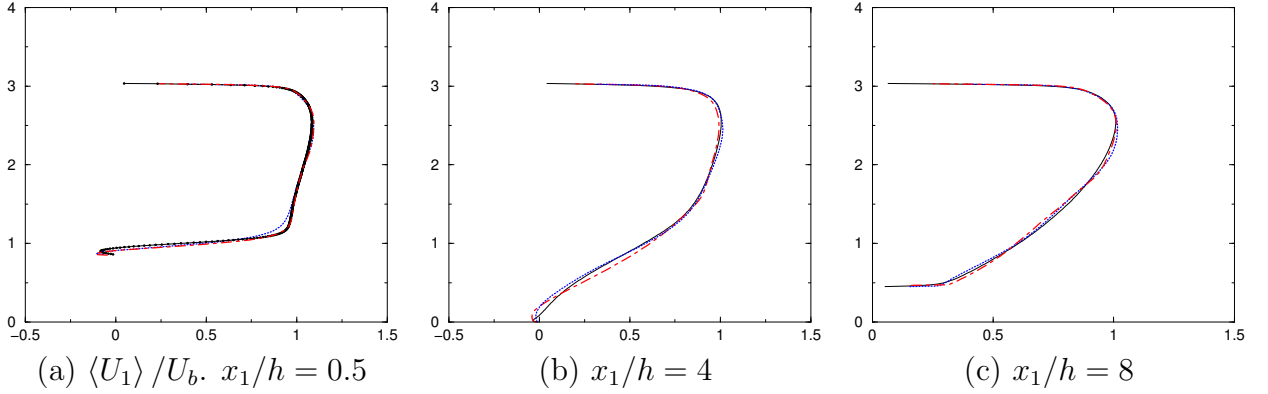


Figure 13. Mean streamwise velocity  $\langle U_1 \rangle / U_b$  at different locations ( $x_1/h = 0.5, 4, 8$ ). LES (Breuer *et al.*, 2009) —; PITM1 ( $80 \times 30 \times 100$ ) ···; PITM2 ( $160 \times 60 \times 100$ ) -.-.

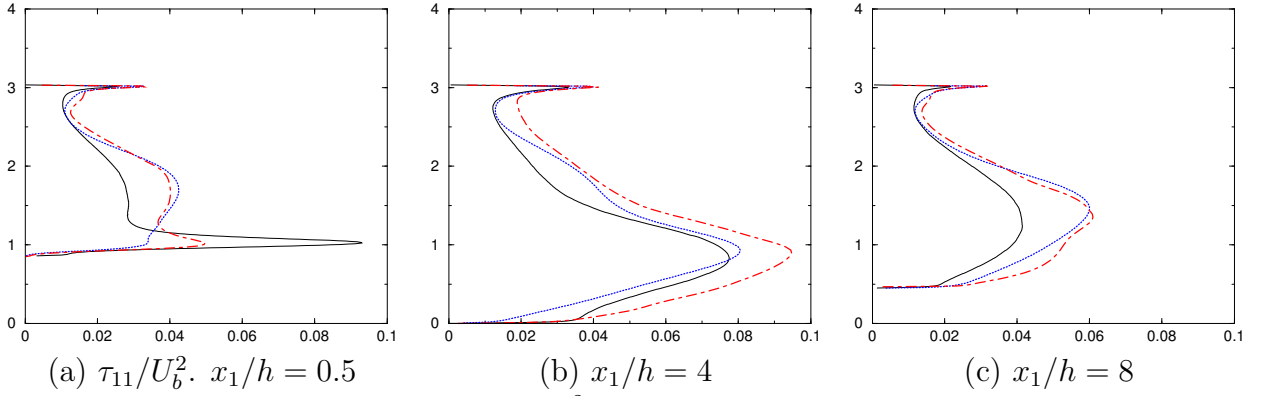


Figure 14. Streamwise turbulent energy  $\tau_{11}/U_b^2$  at different locations ( $x_1/h = 0.5, 4, 8$ ) LES (Breuer *et al.*, 2009) —; PITM1 ( $80 \times 30 \times 100$ ) ···; PITM2 ( $160 \times 60 \times 100$ ) -.-.

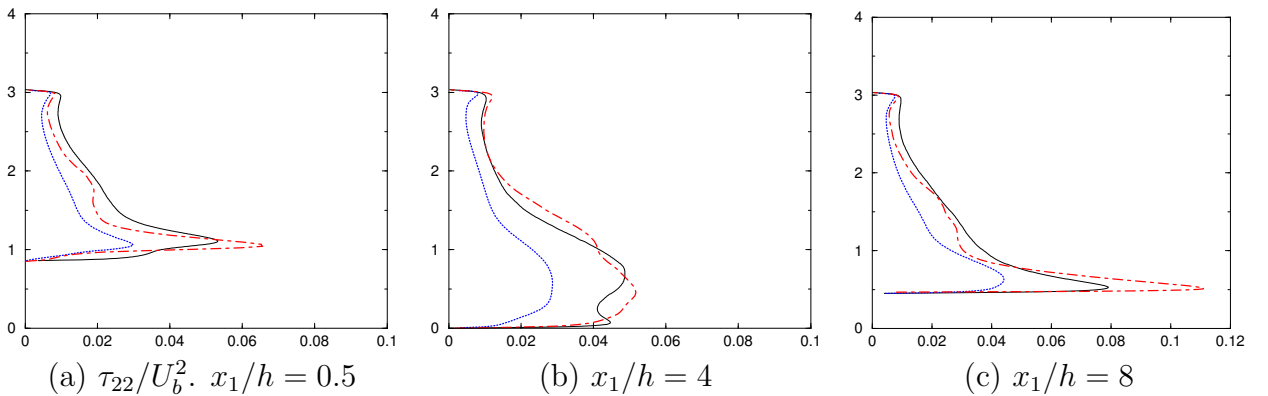


Figure 15. Spanwise turbulent energy  $\tau_{22}/U_b^2$  at different locations ( $x_1/h = 0.5, 4, 8$ ) LES (Breuer *et al.*, 2009) —; PITM1 ( $80 \times 30 \times 100$ ) ···; PITM2 ( $160 \times 60 \times 100$ ) -.-.

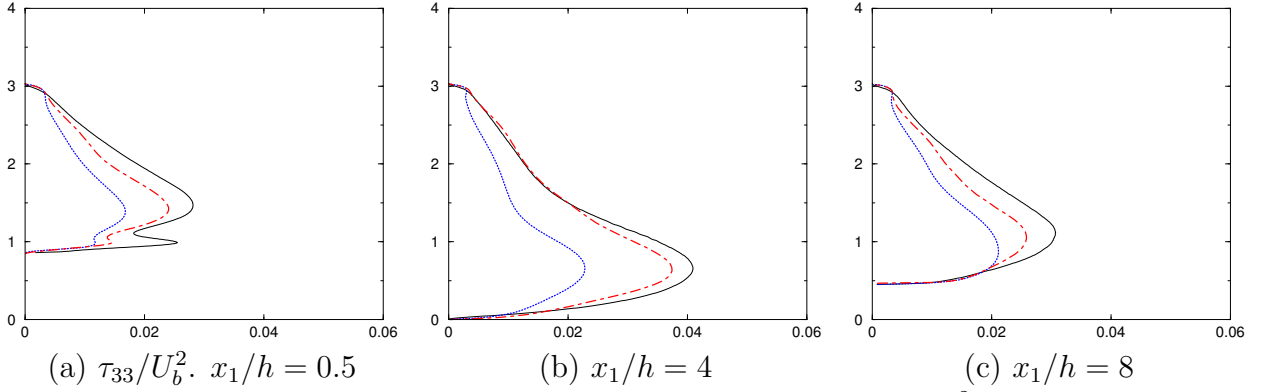


Figure 16. Turbulent energy in the normal direction to the walls  $\tau_{33}/U_b^2$  at different locations ( $x_1/h = 0.5, 4, 8$ ) LES (Breuer *et al.*, 2009) —; PITM1 ( $80 \times 30 \times 100$ )  $\cdots$ ; PITM2 ( $160 \times 60 \times 100$ )  $-\cdots$

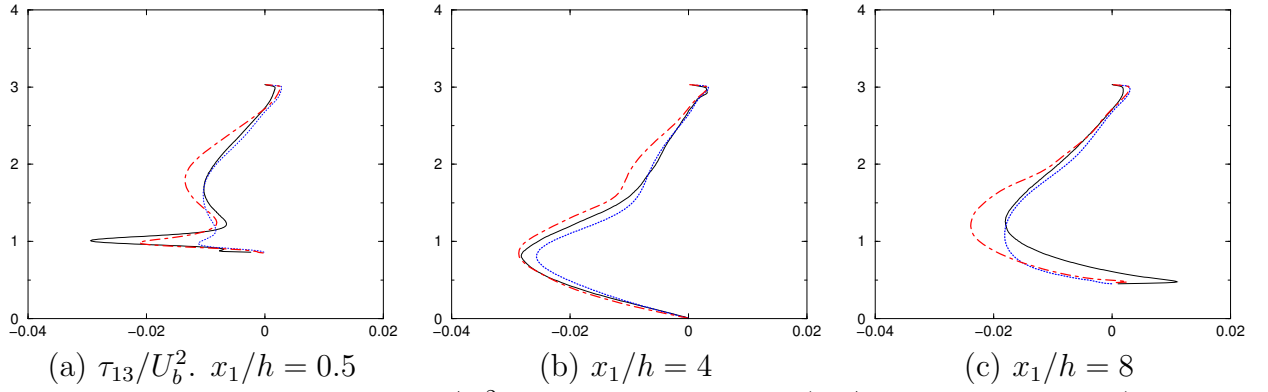


Figure 17. Turbulent shear stress  $\tau_{13}/U_b^2$  at different locations ( $x_1/h = 0.5, 4, 8$ ) LES (Breuer *et al.*, 2009) —; PITM1 ( $80 \times 30 \times 100$ )  $\cdots$ ; PITM2 ( $160 \times 60 \times 100$ )  $-\cdots$

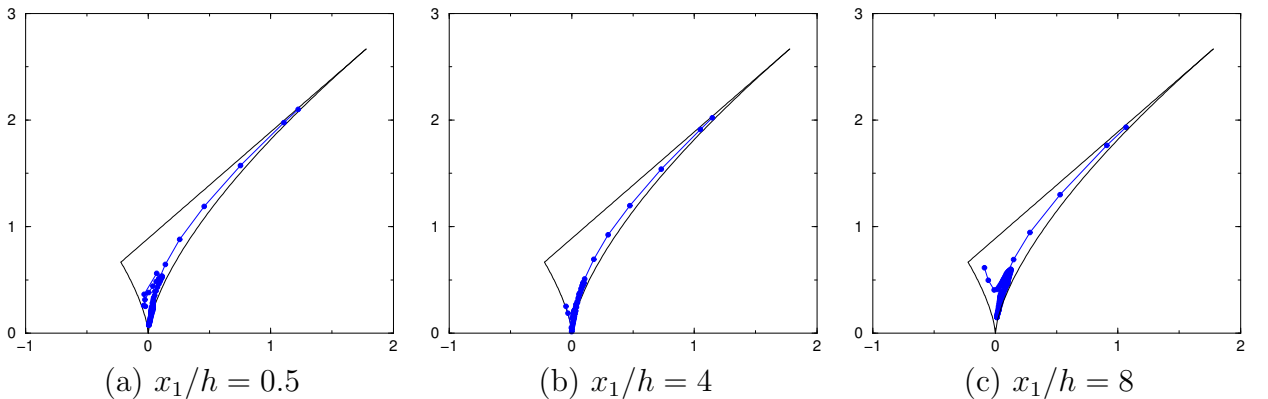


Figure 18. Solution trajectories along vertical lines in the normal direction to the wall at different locations at  $x/h = 0.5, 4, 8$ . projected onto the second-subfilter-invariant/third-subfilter invariant plane

the coarse grid resolutions in the streamwise direction are however observed behind the second hill crest. Figure 13 describes the PITM velocity profiles at three locations  $x/h = 0.5, 4, 8$  of the channel. Although the present grids are of coarse resolution in comparison with refined grids used for performing highly resolved LES [40, 41], the mean velocities agree well with the data of Breuer et al. [41]. But as it could be expected, a better agreement with the reference data is obtained for the PITM2 simulation. These slight differences observed between these two PITM mean velocity profiles must be attributed to the grid size which is not sufficiently refined in the streamwise direction. Figures 14, 15, and 16 display the profiles of the streamwise, spanwise and normal turbulent stresses  $\tau_{11}/U_b^2$ ,  $\tau_{22}/U_b^2$  and  $\tau_{33}/U_b^2$ , respectively, at different locations for both PITM simulations. A first sight reveals that the subfilter model returns turbulent stresses in relatively good agreement with the reference data for almost all positions. As a result of interest, one can see that the turbulent peaks appearing in the boundary layer for the streamwise stresses  $\tau_{11}$  and normal stresses  $\tau_{22}$  at the station  $x_1/h = 0.5$  are well captured by the PITM2 simulation performed on the medium grid but not by the PITM1 simulation performed on the coarse grid. As expected, the PITM2 simulation provides better results than the PITM1 simulation thanks to the grid refinement in the streamwise and spanwise directions that allows a better flow resolution. Figure 17 shows the turbulent shear stress  $\tau_{13}/U_b^2$  profiles at different positions of the channel. Both PITM simulations provide shear stresses that agree well with the reference data. As shown for the normal stresses, the turbulent peak occurring at the stations  $x_1/h = 0.5$  in the boundary layer of the lower wall is well reproduced by the PITM2 simulation but not by the PITM1 simulation. We have demonstrated in the preceding section that the algorithm (31) satisfies the weak form of the realizability conditions. We propose to check the strong form of realizability for particular cases of trajectories by using the diagram of Lumley [42]. Indeed, Lumley has shown that the possible turbulence states must remain inside a curvilinear triangle delimited by the straight line of the two-dimensional state of equation  $A_3 - A_2 + 8/9 = 0$  and by two curves of axisymmetric states of equations  $|A_2| = 6^{1/3} A_3^{2/3}$  where  $A_2$  and  $A_3$  denote the second and third subfilter-scale invariants defined by  $A_2 = a_{ij}a_{ji}$ ,  $A_3 = a_{ij}a_{jk}a_{ki}$  and  $a_{ij} = ((\tau_{ij})_{sfs} - \frac{2}{3}k_{sfs}\delta_{ij})/k_{sfs}$ . Figure 18 displays the computed trajectories along a straight line normal to the wall in three different cross sections of the channel located at  $x/h = 0.5, 4, 8$ . As expected, the solution trajectories remain inside the curvilinear triangle of realizability, confirming that the strong form of realizability conditions defined by Schumann [43] are perfectly satisfied in a mathematical sense by the numerical stress solver.

## 5 Conclusion

We have proposed a numerical method for performing hybrid non-zonal RANS/LES simulations by using second-moment turbulence closures in the approach of finite volume technique. We have applied a fourth order Runge-Kutta scheme for integrating in time the governing equations and we have especially developed iterative algorithms for solving implicitly the turbulent equations. Furthermore, we have demonstrated, in a mathematical sense, that the algorithm satisfies the weak form of realizability. An efficient LES solver of low computational cost has been also developed in space for integrating the system of Navier-Stokes equations and turbulent equations. The numerical method has been calibrated on the decay of homogeneous turbulence and on the fully developed

turbulent channel flow. The complex flow over periodic hills in a constricted channel has been then simulated for illustrating the potentialities of the solver. As a practical result, this work shows that this numerical solver can be easily implemented in CFD codes for performing LES simulations using second-moment closures without dramatically increase the computational cost.

## A Functional coefficients used in the subfilter stress model

The model [3] is based on the transport equations (10) and (16) is developed in a low Reynolds number formulation using damping functions dependent on the Reynolds number  $R_t = k_{sfs}^2/(\nu\epsilon_{sfs})$ , the second and third invariants  $A_2 = a_{ij}a_{ji}$ ,  $A_3 = a_{ij}a_{jk}a_{ki}$  and the flatness parameter  $A = 1 - \frac{9}{8}(A_2 - A_3)$  where  $a_{ij} = ((\tau_{ij})_{sfs} - \frac{2}{3}k_{sfs}\delta_{ij})/k_{sfs}$ . The wall redistribution term is modeled by [22]

$$\begin{aligned} \Psi_{ij}^3 &= c_{1w}\bar{\rho}\frac{\epsilon_{sfs}}{k_{sfs}}((\tau_{kl})_{sfs}n_k n_l \delta_{ij} - \frac{3}{2}(\tau_{ki})_{sfs}n_k n_j - \frac{3}{2}(\tau_{kj})_{sfs}n_k n_i) f_w \\ &+ c_{2w}\left(\Psi_{kl}^2 n_k n_l \delta_{ij} - \frac{3}{2}\Psi_{ik}^2 n_k n_j - \frac{3}{2}\Psi_{jk}^2 n_k n_i\right) f_w \end{aligned} \quad (66)$$

where  $n_i$  is the unit vector perpendicular to the wall, and  $f_w$  is a near wall damping function. The

Functions	Expressions
$c_1$	$1 + 2.58AA_2^{1/4} [1 - \exp(-(R_t/150)^2)](1 + \alpha_{\eta 1} \eta_c^2)/(1 + \alpha_{\eta 2} \eta_c^2)$
$c_2$	$0.6A^{1/2}$
$c_{\epsilon 1}$	1.45
$c_{\epsilon 2}$	1.90
$c_{sfs\epsilon 2}$	$c_{\epsilon 1} + [(c_{\epsilon 2} - c_{\epsilon 1})/(1 + \beta_{\eta} \eta_c^3)^{2/9}]$
$\eta_c$	$\kappa_c k^{3/2}/[(\epsilon_{sfs} + \epsilon^<)]$
$\kappa_c$	$\pi/(\Delta_1 \Delta_2 \Delta_3)^{1/3}$

Table 1: Functions used in subfilter stress model [3].

coefficients used in Table 1 are  $\alpha_{\eta 1} = 1.3/(20)^2$ ,  $\alpha_{\eta 2} = 1/(20)^2$  and  $\beta_{\eta} = [2/(3C_{\kappa})]^{9/2} \approx 0.0495$  for  $C_{\kappa} = 1.3$ . The cutoff wave number function of the grid size is denoted  $\kappa_c$ . The variable  $\epsilon^<$  denotes the dissipation-rate caused by the large-scale fluctuating velocities and  $\Delta_i$  is the filter width in the  $i$ th direction. The wall functions are  $c_{1w} = -\frac{2}{3}c_1 + \frac{5}{3}$ ,  $c_{2w} = \max(\frac{2}{3}c_2 - \frac{1}{6}, 0)/c_2$ ,  $f_w = 0.4k_{sfs}^{3/2}/\epsilon_{sfs}x_n$ . For hybrid/RANS LES simulations,  $c_{sfs\epsilon 2}$  is a dynamical function of the parameter  $\eta_c$  involving the cutoff wave number and the turbulent length-scale.

## B Components of the tensor $t_{ijmn}$

$$\begin{aligned}
t_{1111} &= \alpha_1 \frac{\partial \tilde{u}_1}{\partial x_1} & t_{1112} &= \alpha_2 \left( \frac{\partial \tilde{u}_2}{\partial x_1} + \frac{\partial \tilde{u}_1}{\partial x_2} \right) + \alpha_3 \frac{\partial \tilde{u}_1}{\partial x_2} \\
t_{1113} &= \alpha_2 \left( \frac{\partial \tilde{u}_3}{\partial x_1} + \frac{\partial \tilde{u}_1}{\partial x_3} \right) + \alpha_3 \frac{\partial \tilde{u}_1}{\partial x_3} & t_{1122} &= \alpha_2 \frac{\partial \tilde{u}_2}{\partial x_2} \\
t_{1123} &= \alpha_2 \left( \frac{\partial \tilde{u}_3}{\partial x_2} + \frac{\partial \tilde{u}_2}{\partial x_3} \right) & t_{1133} &= \alpha_2 \frac{\partial \tilde{u}_3}{\partial x_3} \\
t_{2211} &= \alpha_2 \frac{\partial \tilde{u}_1}{\partial x_1} & t_{2212} &= \alpha_2 \left( \frac{\partial \tilde{u}_2}{\partial x_1} + \frac{\partial \tilde{u}_1}{\partial x_2} \right) + \alpha_3 \frac{\partial \tilde{u}_2}{\partial x_1} \\
t_{2213} &= \alpha_2 \left( \frac{\partial \tilde{u}_3}{\partial x_1} + \frac{\partial \tilde{u}_1}{\partial x_3} \right) & t_{2222} &= \alpha_1 \frac{\partial \tilde{u}_2}{\partial x_2} \\
t_{2223} &= \alpha_2 \left( \frac{\partial \tilde{u}_3}{\partial x_2} + \frac{\partial \tilde{u}_2}{\partial x_3} \right) + \alpha_3 \frac{\partial \tilde{u}_2}{\partial x_3} & t_{2233} &= \alpha_2 \frac{\partial \tilde{u}_3}{\partial x_3} \\
t_{3311} &= \alpha_2 \frac{\partial \tilde{u}_1}{\partial x_1} & t_{3312} &= \alpha_2 \left( \frac{\partial \tilde{u}_2}{\partial x_1} + \frac{\partial \tilde{u}_1}{\partial x_2} \right) \\
t_{3313} &= \alpha_2 \left( \frac{\partial \tilde{u}_3}{\partial x_1} + \frac{\partial \tilde{u}_1}{\partial x_3} \right) + \alpha_3 \frac{\partial \tilde{u}_3}{\partial x_1} & t_{3322} &= \alpha_2 \frac{\partial \tilde{u}_2}{\partial x_2} \\
t_{3323} &= \alpha_2 \left( \frac{\partial \tilde{u}_3}{\partial x_2} + \frac{\partial \tilde{u}_2}{\partial x_3} \right) + \alpha_3 \frac{\partial \tilde{u}_3}{\partial x_2} & t_{3333} &= \alpha_1 \frac{\partial \tilde{u}_3}{\partial x_3} \\
t_{1211} &= \alpha_4 \frac{\partial \tilde{u}_2}{\partial x_1} & t_{1212} &= \alpha_4 \left( \frac{\partial \tilde{u}_2}{\partial x_2} + \frac{\partial \tilde{u}_1}{\partial x_1} \right) \\
t_{1213} &= \alpha_4 \frac{\partial \tilde{u}_2}{\partial x_3} & t_{1222} &= \alpha_4 \frac{\partial \tilde{u}_1}{\partial x_2} \\
t_{1223} &= \alpha_4 \frac{\partial \tilde{u}_1}{\partial x_3} & t_{1233} &= 0 \\
t_{1311} &= \alpha_4 \frac{\partial \tilde{u}_3}{\partial x_1} & t_{1312} &= \alpha_4 \frac{\partial \tilde{u}_3}{\partial x_2} \\
t_{1313} &= \alpha_4 \left( \frac{\partial \tilde{u}_1}{\partial x_1} + \frac{\partial \tilde{u}_3}{\partial x_3} \right) & t_{1322} &= 0 \\
t_{1323} &= \alpha_4 \frac{\partial \tilde{u}_1}{\partial x_3} & t_{1333} &= \alpha_4 \frac{\partial \tilde{u}_1}{\partial x_3} \\
t_{2311} &= 0 & t_{2312} &= \alpha_4 \frac{\partial \tilde{u}_3}{\partial x_1} \\
t_{2313} &= \alpha_4 \frac{\partial \tilde{u}_2}{\partial x_1} & t_{2322} &= \alpha_4 \frac{\partial \tilde{u}_3}{\partial x_2} \\
t_{2323} &= \alpha_4 \left( \frac{\partial \tilde{u}_2}{\partial x_2} + \frac{\partial \tilde{u}_3}{\partial x_3} \right) & t_{2333} &= \alpha_4 \frac{\partial \tilde{u}_2}{\partial x_3}
\end{aligned}$$

where  $\alpha_1 = (4c_2 - 6)/3$ ,  $\alpha_2 = -2c_2/3$ ,  $\alpha_3 = 2(c_2 - 1)$ ,  $\alpha_4 = c_2 - 1$ .

## C Expression of the two vectors $\mathbf{r}_+$ , $\mathbf{r}_-$ and the two row vectors $\mathbf{l}^+$ , $\mathbf{l}^-$

The Jacobian matrix is obtained by

$$\mathbf{J} = \frac{\partial \mathbf{F}}{\partial \mathbf{U}} = \frac{\partial}{\partial \mathbf{U}} (\tilde{u}_m n_m \mathbf{U} + \bar{p} \mathbf{V}) \quad (67)$$

where  $\mathbf{V} = [0, n_1, n_2, n_3, \tilde{u}_m n_m, 0, 0, 0, 0, 0, 0]^T$ . Using the product rule for derivatives, one can easily obtain

$$\mathbf{J} = \tilde{u}_m n_m \mathbf{I} + \mathbf{U} \otimes \frac{\partial(\tilde{u}_m n_m)}{\partial \mathbf{U}} + \bar{p} \frac{\partial \mathbf{V}}{\partial \mathbf{U}} + \mathbf{V} \otimes \frac{\partial \bar{p}}{\partial \mathbf{U}} \quad (68)$$

where  $\mathbf{I}$  is the identity matrix. When developing the calculus, equation (68) can be rearranged into the following form

$$\mathbf{J} = \tilde{u}_m n_m \mathbf{I} + c (\mathbf{r}_a \otimes \mathbf{l}^b + \mathbf{r}_b \otimes \mathbf{l}^a) \quad (69)$$

where the two vectors  $\mathbf{r}_a$  and  $\mathbf{r}_b$  and the two row vectors  $\mathbf{l}^a$  and  $\mathbf{l}^b$  are defined by

$$\mathbf{r}_a = \begin{bmatrix} 1 \\ \tilde{u}_1 \\ \tilde{u}_2 \\ \tilde{u}_3 \\ \tilde{H} \\ (\tau_{11})_{sfs} \\ (\tau_{12})_{sfs} \\ (\tau_{13})_{sfs} \\ (\tau_{22})_{sfs} \\ (\tau_{23})_{sfs} \\ (\tau_{33})_{sfs} \\ \epsilon_{sfs} \end{bmatrix}, \quad \mathbf{r}_b = \begin{bmatrix} 0 \\ c n_1 \\ c n_2 \\ c n_3 \\ c \tilde{u}_m n_m \\ 0 \\ 0 \\ 0 \\ 0 \\ 0 \\ 0 \\ 0 \end{bmatrix},$$

$$\mathbf{l}^a = \frac{\gamma - 1}{c^2} \left[ \frac{\tilde{u}_m \tilde{u}_m}{2}, -\tilde{u}_1, -\tilde{u}_2, -\tilde{u}_3, 1, -\frac{1}{2}, 0, 0, -\frac{1}{2}, 0, -\frac{1}{2}, 0 \right],$$

and

$$\mathbf{l}^b = \frac{1}{c} [-\tilde{u}_m n_m, n_1, n_2, n_3, 0, 0, 0, 0, 0, 0, 0, 0],$$

verifying the remarkable orthogonality relations

$$\mathbf{l}^a \mathbf{r}_a = \mathbf{l}^b \mathbf{r}_b = 1 \quad (70)$$

and

$$\mathbf{l}^a \mathbf{r}_b = \mathbf{l}^b \mathbf{r}_a = 0 \quad (71)$$

Lets define the vectors  $\mathbf{r}_+ = \mathbf{r}_a + \mathbf{r}_b$ ,  $\mathbf{r}_- = \mathbf{r}_a - \mathbf{r}_b$ ,  $\mathbf{l}^+ = (\mathbf{l}^a + \mathbf{l}^b)/2$  and  $\mathbf{l}^- = (\mathbf{l}^a - \mathbf{l}^b)/2$ , using equations (70) and (71), one can remark that

$$\mathbf{J}(\mathbf{r}_+) = (u_m n_m + c) \mathbf{r}_+ \quad (72)$$

$$\mathbf{J}(\mathbf{r}_-) = (u_m n_m - c) \mathbf{r}_- \quad (73)$$

and

$$(\mathbf{l}^+) \mathbf{J} = \mathbf{l}^+ (u_m n_m + c) \quad (74)$$

$$(\mathbf{l}^-) \mathbf{J} = \mathbf{l}^- (u_m n_m - c) \quad (75)$$

showing that  $\mathbf{r}_+$ ,  $\mathbf{r}_-$  and  $\mathbf{l}^+$ ,  $\mathbf{l}^-$  are the right and left eigenvectors of the Jacobian matrix  $\mathbf{J}$  with the corresponding eigenvalues.

## D Matrix spectral decomposition

Lets consider the matrices  $\mathbf{A}$ ,  $\mathbf{P}$  and  $\mathbf{Q}$  of dimension  $n$  such as  $\mathbf{A} = \mathbf{P}\mathbf{\Lambda}\mathbf{Q}$  where  $\mathbf{P}$  and  $\mathbf{Q} = \mathbf{P}^{-1}$  denote the transformation matrices and  $\mathbf{\Lambda}$  is the diagonalizable matrix with  $n$   $\lambda_i$  eigenvalues. Then, the matrix  $A$

$$\mathbf{A} = \begin{pmatrix} a_{11} & a_{12} & \dots & a_{1n} \\ a_{21} & a_{22} & \dots & a_{2n} \\ \vdots & \vdots & \ddots & \vdots \\ a_{n1} & a_{n2} & \dots & a_{nn} \end{pmatrix}$$

where  $a_{ij} = p_{ik} \lambda_k q_{kj}$  can be rewritten in the base of eigenvectors under a spectral decomposition form as follows

$$\mathbf{A} = \lambda_1 \begin{pmatrix} p_{11} \\ p_{21} \\ \vdots \\ p_{n1} \end{pmatrix} \otimes ( q_{11} \quad q_{12} \quad \dots \quad q_{1n} ) + \lambda_2 \begin{pmatrix} p_{12} \\ p_{22} \\ \vdots \\ p_{n2} \end{pmatrix} \otimes ( q_{21} \quad q_{22} \quad \dots \quad q_{2n} ) + \dots$$

where  $\mathbf{P}_i$  and  $\mathbf{Q}_i$  are the right and left eigenvectors of the matrix  $\mathbf{A}$  with the corresponding eigenvalue  $\lambda_i$ , respectively.

## References

- [1] R. Schiestel and A. Dejoan. Towards a new partially integrated transport model for coarse grid and unsteady turbulent flow simulations. *Theoretical Computational Fluid Dynamics*, 18:443–468, 2005.
- [2] B. Chaouat and R. Schiestel. A new partially integrated transport model for subgrid-scale stresses and dissipation rate for turbulent developing flows. *Physics of Fluids*, 17(065106):1–19, 2005.
- [3] B. Chaouat and R. Schiestel. Progress in subgrid-scale transport modelling for continuous hybrid non-zonal RANS/LES simulations. *International Journal of Heat and Fluid Flow*, 30:602–616, 2009.
- [4] B. Chaouat and R. Schiestel. From single-scale turbulence models to multiple-scale and subgrid-scale models by Fourier transform. *Theoretical Computational Fluid Dynamics*, 21(3):201–229, 2007.
- [5] R. Schiestel. *Modeling and simulation of turbulent flows*. ISTE Ltd and J. Wiley, 2008.
- [6] P. R. Spalart. Strategies for turbulence modelling and simulations. *International Journal of Heat and Fluid Flow*, 21:252–263, 2000.
- [7] C. L. Rumsey and V. N. Vasta. Comparison of the predictive capabilities of several turbulence models. *Journal of Aircraft*, 32(3):510–514, 1995.
- [8] M. Germano, U. Piomelli, P. Moin, and W. H. Cabot. A dynamic subgrid-scale eddy-viscosity model. *Physics of Fluids*, 3(7):1760–1765, 1992.
- [9] C. L. Rumsey and T. B. Gatski. Recent turbulence model advances applied to multielement airfoil computations. *Journal of Aircraft*, 38(5):904–910, 2001.
- [10] T. B. Gatski, C. L. Rumsey, and R. Manceau. Current trends in modelling research for turbulent aerodynamic flows. *Phil. Trans. Royal Society*, 365:2389–2418, 2007.
- [11] B. E. Launder, G. J. Reece, and W. Rodi. Progress in the development of a Reynolds stress turbulence closure. *Journal of Fluid Mechanics*, 68:537–566, 1975.
- [12] K. Hanjalic and S. Jakirlic. Contribution towards the second-moment closure modeling of separating turbulent flows. *Computers and Fluids*, 27(2):137–156, 1998.
- [13] B. Chaouat. Numerical predictions of channel flows with fluid injection using a Reynolds stress model. *Journal of Propulsion and Power*, 18(2):295–303, 2002.
- [14] B. Chaouat and R. Schiestel. Reynolds stress transport modelling for steady and unsteady channel flows with wall injection. *Journal of Turbulence*, 3:1–15, 2002.
- [15] J. W. Deardorff. The use of subgrid transport equations in a three-dimensional model of atmospheric turbulence. *Journal of Fluid Engineering, ASME*, 95:429–438, 1973.
- [16] K. Hanjalic. Second-moment turbulence closures for CFD: Needs and prospects. *International Journal of Computational Fluid Dynamics*, 12:67–97, 1999.

- [17] G. Barakos and D. Drikakis. Implicit unfactored implementation of two-equation turbulence model in compressible Navier-Stokes methods. *International Journal for Numerical Methods in Fluids*, 28:73–94, 2008.
- [18] D. Gottlieb and S.A. Orzag. *Numerical analysis of spectral methods: Theory and applications*. SIAM, 1977.
- [19] C. Canuto, M.Y. Hussaini, A. Quarteroni, and T. A. Zang. *Spectral Methods in Fluids Dynamics*. Springer-Verlag, 1988.
- [20] S. K. Lele. Compact finite difference schemes with spectral-like resolution. *Journal of Computational Physics*, 103:16–42, 1992.
- [21] R. Eymard, T. Gallouet, and R. Herbin. *Finite volume methods*. Handbook of numerical analysis, 1999.
- [22] M. M. Gibson and B. E. Launder. Ground effects on pressure fluctuations in the atmospheric boundary layer. *Journal of Fluid Mechanics*, 86:491–511, 1978.
- [23] R. Schiestel. Sur le concept d'échelles multiples en modélisation des écoulements turbulents. part I. *Journal de Mécanique Théorique et Appliqué*, 2(3):417–449, 1983.
- [24] R. Schiestel. Sur le concept d'échelles multiples en modélisation des écoulements turbulents. part II. *Journal de Mécanique Théorique et Appliqué*, 2(4):601–628, 1983.
- [25] B. Chaouat. Simulations of channel flows with effects of spanwise rotation or wall injection using a Reynolds stress model. *Journal of Fluid Engineering, ASME*, 123:2–10, 2001.
- [26] C. Hirsch. *Numerical computation of Internal and External Flows*. John Willey, 1988.
- [27] C. G. Speziale, R. Abid, and P. A. Durbin. On the realisability of Reynolds stress turbulence closures. *Journal of Scientific Computing*, 9(4):369–403, 1994.
- [28] R. Schiestel and B. Chaouat. On partially integrated transport models for subgrid-scale modelling. *ERCRAFTAC Bulletin*, 72:49–54, 2007.
- [29] P. L. Roe. Approximate Riemann solvers, parameter vectors and difference schemes. *Journal of Computational Physics*, 43:357–372, 1981.
- [30] C. L. Rumsey, B. Van Leer, and P. L. Roe. A multidimensional flux function with applications to the Euler and Navier-Stokes equations. *Journal of Computational Physics*, 105:306–323, 1993.
- [31] D. Dutoya and M. P. Errera. A formal decomposition of the jacobian matrix of the Euler equations. application to upwind numerical schemes. *La Recherche Aéronautique*, 1:25–35, 1992.
- [32] B. Vanleer. Towards the ultimate conservative difference scheme (part v). a second order sequel to godunov's method. *Journal of Computational Physics*, 32:101–136, 1979.
- [33] R. Vichnevetsky and J. B. Bowles. *Fourier analysis of numerical approximations of hyperbolic equations*. SIAM Philadelphia, 1982.
- [34] B. Thornber, D. Drikakis, R. J. R. Williams, and D. Youngs. On entropy generation and dissipation of kinetic energy in high-resolution shock-capturing schemes. *Journal of Computational Physics*, 227:4853–4872, 2008.

- [35] S. Bhushan and Z. U. A. Warsi. Large eddy simulation of turbulent channel flow using an algebraic model. *International Journal for Numerical Methods in Fluids*, 49:399–519, 2005.
- [36] B. Thornber, A. Mosedale, and D. Drikakis. On the implicit large eddy simulations of homogeneous decaying turbulence. *Journal of Computational Physics*, 226:1902–1929, 2007.
- [37] Ph. Roy. Résolution des équations de Navier-Stokes par un schéma de haute précision en espace et en temps. *La Recherche Aéronautique*, 6:373–385, 1980.
- [38] Y. Dubief and F. Delcayre. On coherent-vortex identification in turbulence. *Journal of Turbulence*, 1(11):1–22, 2000.
- [39] R. Moser, D. Kim, and N. Mansour. Direct numerical simulation of turbulent channel flow up to  $R_\tau = 590$ . *Physics of Fluids*, 11(4):943–945, 1999.
- [40] J. Fröhlich, C. Mellen, W. Rodi, L. Temmerman, and M. Leschziner. Highly resolved large-eddy simulation of separated flow in a channel with streamwise periodic constriction. *Journal of Fluid Mechanics*, 526:19–66, 2005.
- [41] M. Breuer, N. Peller, Ch. Rapp, and M. Manhart. Flow over periodic hills. Numerical and experimental study in a wide range of Reynolds numbers. *Computers and Fluids*, 38:433–457, 2009.
- [42] J. L. Lumley. Computational modeling of turbulent flows. *Advances in Applied Mechanics*, 18:123–176, 1978.
- [43] U. Schumann. Realizability of Reynolds stress turbulence models. *Physics of Fluids*, 20(5):721–725, 1977.